

The star formation history of luminous infrared galaxies

D. Marcillac^{1,8}, D. Elbaz¹, S. Charlot^{2,3}, Y. C. Liang^{4,5}, F. Hammer⁵, H. Flores⁵, C. Cesarsky⁶, A. Pasquali⁷

¹ DSM/DAPNIA/Service d'Astrophysique, CEA/SACLAY, 91191 Gif-sur-Yvette Cedex, France
e-mail: marcilla, elbaz@cea.fr

² Max-Planck-Institut für Astrophysik, Karl-Schwarzschild-Strasse 1, Garching D-85748, Germany

³ Institut d'Astrophysique de Paris, CNRS, 98 bis Boulevard Arago, Paris 75014, France
e-mail: charlot@iap.fr

⁴ National Astronomical Observatories, Chinese Academy of Sciences, No.20A Datun Road, Chaoyang District, Beijing 100012, P. R. China
e-mail: ycliang@bao.ac.cn

⁵ GEPI, Observatoire de Paris, Section de Meudon, 92195 Meudon Cedex, France
e-mail: hector.flores, francois.hammer@obspm.fr

⁶ ESO, Karl-Schwarzschild Strasse 2, D85748 Garching bei Munchen, Germany
e-mail: ccesarsk@eso.org

⁷ Max-Planck-Institut fuer Astronomie, Koenigstuhl 17, D-69117 Heidelberg, Germany
e-mail: pasquali@phys.ethz.ch

⁸ Current address: Steward Observatory, University of Arizona, 933, N. Cherry Avenue, Tucson, AZ 85721, USA
e-mail: dmarci@as.arizona.edu

Received ...; accepted ...

ABSTRACT

Aims. We constrain the past star formation histories of a sample of 25 distant ($z \sim 0.7$) luminous infrared galaxies (LIRGs) detected with the mid infrared cameras ISOCAM and MIPS onboard the ISO and Spitzer satellites.

Methods. We use high resolution VLT-FORS2 spectroscopy in addition to a comprehensive library of 200,000 model optical spectra to derive Bayesian likelihood estimates of the star formation histories of these galaxies based on the analysis of Balmer absorption lines and the 4000 Å break.

Results. The locus of distant LIRGs in the diagram defined by $H\delta_A$ and D4000 is roughly comparable to that of local LIRGs observed with IRAS, suggesting that no trend for an evolution is detected between the local and distant LIRGs. We obtain similar results when using either the H8 or the $H\delta_A$ Balmer absorption-line indices in combination with D4000.

We compute a birthrate parameter ($b = \text{SFR} / \langle \text{SFR} \rangle$) of 4 ± 1 , confirming that the distant LIRGs are currently experiencing a major phase of star formation. The most likely duration of the bursts is $0.10^{+0.16}_{-0.06}$ Gyr, during which the LIRGs produce ~ 5 -10% of their current stellar mass. No evidence is found for successive starbursts on the scale of a few times 10^7 yr, such as those predicted by some numerical simulations of major mergers. However, the large number density of those galaxies suggest that they could experience between two and four LIRG phases until the present epoch. This scenario is not consistent with the formation of the $z \sim 0.7$ LIRGs through the continuous star formation characterizing isolated spiral galaxies as has been argued independently based on their morphology. Instead, minor mergers, tidal interactions or gas accretion remain plausible triggering mechanisms for more than half of the distant LIRGs which do not harbor the morphology of major mergers.

Key words. Galaxies: evolution – Infrared: galaxies – Galaxies: starburst

1. Introduction

Luminous infrared (IR) galaxies, i.e. galaxies radiating more than $\sim 90\%$ of their light above $5 \mu\text{m}$, have been suggested to provide important constraints on galaxy formation and evolution. They are considered to be the main cause of the cosmic infrared background (CIRB) and major contributors to the evo-

lution with redshift of the cosmic star formation rate (CSFR) of galaxies (Elbaz et al. 2002, Chary & Elbaz 2001, see also the review by Lagache *et al.* 2005). The role of luminous IR galaxies (LIRGs for $10^{11} L_{\odot} \leq L_{\text{IR}} = L[8-1000 \mu\text{m}] < 10^{12} L_{\odot}$) and ultra-luminous IR galaxies (ULIRGs for $L_{\text{IR}} \geq 10^{12} L_{\odot}$) in the local universe could be neglected since they only produce about 6% of the integrated IR emission of local galaxies, hence 2% of their bolometric luminosity (Soifer & Neugebauer 1991). But they rapidly evolve with redshift and dominate the CSFR above

Send offprint requests to: D. Marcillac, email: marcilla@as.arizona.edu

$z \sim 0.6$ (Le Floc’h et al. 2005). IRAS extragalactic surveys already suggested that their number density evolved rapidly with redshift ($\sim (1+z)^{7.6\pm 3.2}$ up to $z \sim 0.2$; Kim & Sanders, 1998). This rapid evolution was later on confirmed up to $z \sim 1$ with ISOCAM and ISOPHOT onboard ISO at 15 and 170 μm (see Elbaz et al. 2005 and references therein), above $z \sim 2$ using SCUBA at 850 μm (Smail et al. 2001, Blain et al. 1999) and in the intermediate redshift range with MIPS onboard Spitzer at 24 μm (Chary et al. 2004, Papovitch et al. 2004, Le Floc’h et al. 2005). However, little is known about the characteristics of the starbursts themselves, e.g. the amount of stars born during the burst, the burst duration, and even less about the physical processes responsible for the intense activity of these galaxies. One of the major reasons for this lack of information comes from their nature itself, i.e. the strong dust obscuration of their optical light.

In a previous paper (Liang et al. 2004, hereafter Paper I), we presented an analysis of the emission line properties of the galaxies. The star formation rates (SFR) derived from the Balmer emission lines ($H\alpha$ and/or $H\beta$, plus $H\gamma$ to derive dust attenuations) were corrected for dust attenuation and found to be consistent with the ones derived from the mid IR (MIR) using the technique described in Chary & Elbaz (2001). This study showed that LIRGs in general are not completely obscured by dust and that the use of high-resolution optical spectroscopy ($\Delta\lambda/\lambda = 2000$, in the rest-frame of the objects) could be used to derive intrinsic luminosities, hence SFR, in rough agreement with the IR-derived SFR, by minimizing the contamination by sky emission lines and allowing to better correct for underlying photospheric absorption lines. However, the consistent derivation of the signal-to-noise ratio on the intrinsic luminosities lead to large uncertainties on the measured visual attenuation. Moreover, there is evidence for some completely obscured star formation as found in the most luminous objects studied in Flores et al. (2004) or in Cardiel et al. (2003). The limited statistics of those studies clearly calls for an extension of the sample of distant LIRGs, with good S/N on the optical continuum and high spectral resolution, to robustly determine which fraction of the star formation taking place in LIRGs and ULIRGs is completely obscured by dust. However Hopkins *et al.* (2003) showed that SFR([OII]), SFR(1.4 GHz), and SFR(FIR) are in very good agreement for a larger sample of local infrared galaxies detected with IRAS and spectroscopically observed with the Sloan Digital Sky Survey (SDSS).

In the present paper, we wish to address the problem from another angle: stars less massive, hence with longer lifetimes, than those responsible for the emission lines standardly used to derive the optical SFR of galaxies can escape their parent giant molecular cloud (GMC) and their spectral signature might be used to derive key parameters concerning the starburst. The $H\alpha$ light used to derive a SFR is dominantly produced by the ionizing photons arising from stars more massive than $\sim 10 M_{\odot}$, with lifetimes shorter than 3 Myr. Those stars never escape their parent GMC (average lifetime of 10 Myr) and the dense regions of very strong extinction, contrary to the A and F stars which are the main contributors to the Balmer absorption lines and the 4000 \AA break.

We use these signatures of the optical continuum to compare distant LIRGs to nearby IRAS galaxies or synthetic spectra generated with the Bruzual & Charlot (2003) model. We find a signature of the starbursts in the D4000- $H\delta$ diagram and use it to derive the burst properties.

Paper I indirectly confirmed the strong role played by LIRGs in the CSFR history with the derivation of gas metallicities in distant LIRGs twice smaller than the one measured in present-day galaxies of equal absolute B band magnitude. This result suggested that these galaxies produced about half of their metals between $z \sim 1$ and today. It was also suggested that such a large metal production, as well as the large contribution of LIRGs to the CSFR and CIRB, could not result from a single burst phase in the galaxies harboring LIRG phases and hence that those galaxies must have experienced a series of LIRG phases in their lifetime. This possibility is tested in the present paper.

Finally we note that, based on optical spectra, no evidence was found in Paper I for a dominant contribution from active galactic nuclei (AGNs) in the sample of 76 distant LIRGs for which a spectroscopic redshift was determined. This confirmed the previous result from Fadda et al. (2001) that AGNs were contributing to less than 20 % of the MIR light of distant LIRGs, as shown by their soft to hard X-ray radiation measured with the Newton and Chandra X-ray observatories.

In this paper, we study the stellar spectra of a sample of 25 LIRGs with a median redshift of $\bar{z} = 0.7$ using high-resolution spectroscopy with the FORS2 instrument at the VLT ($\Delta\lambda/\lambda = 1200$, equivalent to 2000 in the rest-frame of the galaxies). This sample is smaller than in Paper I because higher signal-to-noise ratios are required to study the continuum emission in comparison to the emission lines. All galaxies are detected at 15 μm with ISOCAM and the 11 galaxies located in one of the three fields are also detected at 24 μm with the MIPS camera onboard Spitzer (Papovich et al. 2004, Elbaz et al. 2005). We show that both indicators provide consistent estimates of the total IR luminosity of the galaxies, hence also the SFR (see also Elbaz et al. 2005, Marcillac et al. 2005 for a more detailed study).

Sect.2 presents the sample selection and the wavelet decomposition technique that we used to analyze the spectra. Sect.3 describes the method used in this paper to study the SFR history of the galaxies, namely the Balmer absorption line $H\delta_A$ (4101 \AA) versus 4000 \AA break position of the galaxies, as previously done by Kauffmann et al. (2003) for the Sloan Digital Sky Survey (SDSS). We extended the method used in Kauffmann et al. (2003) to the high order Balmer line H8 (3889 \AA) and H9 (3835 \AA) which are easier to detect in distant galaxies due to the k-correction. The comparison of local and distant LIRGs in this parameter space is discussed in Sect.4 while the model used to generate Monte Carlo realizations of 200,000 spectra with different star formation histories is presented in Sect.5. The results are presented in Sect.6 and discussed in the last Section.

Throughout this paper, we will assume $H_0 = 75 \text{ km s}^{-1} \text{ Mpc}^{-1}$, $\Omega_{\text{matter}} = 0.3$ and $\Omega_{\Lambda} = 0.7$.

Object Slit (1)	RA (J2000) (2)	DEC (J2000) (3)	z (4)	H8 (5)	H δ_A (6)	D4000 (7)	F $_v^{15\mu\text{m}}$ μJy (8)	F $_v^{24\mu\text{m}}$ μJy (9)	log($\frac{L_{\text{IR}}}{L_{\odot}}$) (10)	SFR $_{\text{IR}}$ $M_{\odot} \text{ yr}^{-1}$ (11)
UDSR08	3 14 55.20	-55 20 31.0	0.7291	3.8±0.5	4.2 ± 0.9	1.11±0.02	236±75	–	11.44±0.24	46.7
UDSR09	3 14 56.10	-55 20 08.0	0.3884	1.4±0.4	–	1.74±0.03	609±87	–	11.20±0.08	27.2
UDSR10	3 14 43.90	-55 21 35.0	0.6798	4.3±0.6	8.4 ± 0.7	1.25±0.03	495±91	–	11.78±0.13	102.9
UDSR14	3 14 43.30	-55 20 11.0	0.8150	4.7±0.4	3.9 ± 0.4	1.15±0.02	200±69	–	11.48±0.27	52.0
UDSR20	3 14 41.10	-55 18 40.0	0.7660	6.9±0.5	6.5 ± 0.8	1.19±0.02	214±72	–	11.44±0.25	47.0
UDSR23	3 14 32.10	-55 19 02.0	0.7094	4.9±0.4	4.7 ± 0.3	1.15±0.02	271±80	–	11.48±0.22	51.8
UDSF06	3 13 30.20	-55 04 04.0	0.6928	4.3±1.3	–	1.27±0.06	150±75	180±22	11.09±0.49	21.0
UDSF07	3 13 17.30	-55 05 16.0	0.7014	3.6±0.9	4.2 ± 0.7	1.17±0.04	154±32	198±27	11.12±0.15	22.6
UDSF12	3 13 07.70	-55 05 26.0	0.7388	7.6±0.9	–	1.29±0.06	331±58	420±30	11.64±0.11	74.7
UDSF16	3 13 08.0	-55 04 18.0	0.4548	–	3.7±0.6	1.25±0.01	138±29	205±26	10.55±0.11	6.0
UDSF17	3 13 08.60	-55 03 57.0	0.8100	6.2±0.3	6.7 ± 0.4	1.22±0.02	257±47	343±23	11.62±0.12	72.0
UDSF18	3 13 16.5	-55 02 27.0	0.4620	–	4.7 ± 0.8	1.17 ± 0.1	170±44	–	10.68±0.10	8.2
UDSF19	3 13 09.80	-55 03 08.0	0.5476	4.8±1.0	3.9 ± 1.2	1.32±0.05	611±90	778±40	11.62±0.09	71.4
UDSF28	3 12 51.80	-55 02 57.0	0.6612	2.9±0.6	–	1.47±0.04	321±35	861±37	11.49±0.06	53.1
UDSF29	3 12 50.20	-55 02 59.0	0.6619	4.1±1.3	–	1.37±0.06	354±66	568±28	11.54±0.11	59.6
UDSF20	3 13 19.00	-55 01 42.0	0.8424	2.8±0.7	–	1.33±0.04	117±25	248±21	11.19±0.16	26.7
UDSF31	3 12 44.00	-55 03 21.0	0.6868	4.5±1.1	5.6± 1.1	1.44±0.06	193±38	174±28	11.24±0.14	29.9
CFRS02	3 02 52.01	+00 10 33.0	0.6172	6.9±1.0	5.9± 1.2	1.30±0.10	582±114	–	11.75±0.12	95.8
CFRS06	3 02 49.08	+00 10 1.8	0.6169	3.8±0.4	5.0± 0.3	1.21±0.02	370±95	–	11.50±0.17	53.5
CFRS08	3 02 46.29	+00 13 53.6	0.7154	4.0±0.3	5.9± 0.9	1.24±0.03	360±95	–	11.65±0.17	75.7
CFRS10	3 02 44.57	+00 12 20.1	0.5276	5.6±0.6	5.9± 1.2	1.03±0.04	220±95	–	11.01±0.40	17.7
CFRS11	3 02 42.31	+00 12 9.5	0.6895	–	2.5± 0.7	1.15±0.04	425±110	–	11.70±0.16	85.4
CFRS14	3 02 40.44	+00 14 3.8	0.4652	4.6±0.5	6.5± 0.5	1.10±0.02	172±117	–	10.69±0.58	8.4
CFRS16	3 02 38.80	+00 14 17.5	0.8274	3.3±1.0	–	1.30±0.05	444±100	–	11.99±0.15	166.7
CFRS29	3 02 29.41	+00 12 59.8	0.8804	7.3±1.4	–	1.13±0.05	370±103	–	11.98±0.20	163.6

Table 1. Description of the distant LIRGs sample. The technique used to compute the equivalent widths of $H\delta$, $H8$, $H9$, $H10$ and the 4000 Å break ($D4000$) is described in Sect. 2.3. L_{IR} and SFR_{IR} were derived using the Chary & Elbaz (2001) technique.

2. Sample selection and data reduction

2.1. Sample selection

The sample of distant LIRGs was selected from three deep ISOCAM $15\mu\text{m}$ surveys and is described in Paper I. 105 galaxies were selected on the basis of their $15\mu\text{m}$ flux density in three different regions of the southern hemisphere, hence avoiding strong contamination by cosmic variance: the ISOCAM Ultra-Deep Surveys in the FIRBACK (UDSF) and ROSAT (UDSR) fields and the CFRS 3^h field. All three fields were selected for their low cirrus contamination and high galactic latitude. The UDSF ($9'\times 9'$) is located at the center of the “far infrared background” survey at $175\mu\text{m}$ with ISOPHOT onboard ISO (‘FIRBACK’; Puget et al. 1999, Lagache & Dole 2001). The UDSR is centered at the position of a deep ROSAT survey (Zamorani et al. 1999). The UDSR and UDSF are both close to the position of the so-called ‘Marano Field’ originally selected for an optical survey of quasars (Marano et al. 1988), but are separated by $21'$ with respect to each other. The third field is one of the Canada France Redshift Survey fields (CFRS 3^h) combining deep infrared, optical and radio data as well as spectra from the MOS multiobject spectrograph on the 3.6m CFHT.

ISOCAM sources were selected to span the whole flux density range of the three surveys whose 80% completeness limits are $150\mu\text{Jy}$ for the UDSF and UDSR and $250\mu\text{Jy}$ for the CFRS 3^h , while the detection limits are $50\mu\text{Jy}$ (UDSF, UDSR)

and $170\mu\text{Jy}$ (faintest sources in the regime below completeness). No optical selection was applied so that the magnitudes of the sources range from $R_{\text{AB}} = 19.4$ to 23.7 . At about the same epoch (November 2003) than the VLT-FORS2 observations, a $24\mu\text{m}$ survey was being performed with the MIPS camera onboard Spitzer during the MIPS commissioning phase (IOC/SV). This survey covers the whole UDSF field and all eleven ISOCAM- $15\mu\text{m}$ sources were detected at $24\mu\text{m}$, i.e. 45% of the sample. The scan map AOT was used, with an half-array overlap to cover about 1300 Sq. Arcmin with high redundancy (20) and to get an integration time per sky pixel of about 230s (Papovich et al. 2004). The data were reduced using the *Spitzer* Science Center Pipeline and the BCD products (Basic Calibrated Data, Pipeline version S10.0.3) were downloaded from the *Spitzer* archive¹. PSF-fitting photometry was performed using DAOPHOT (Stetson 1987) with IRAF².

From a total of 105 galaxies observed with FORS2 at the VLT (Paper I), we detected 3 stars, 13 galaxies were too faint for a redshift determination and within the remaining list, 13 other galaxies were not detected with ISOCAM. The resulting list of 76 galaxies with a MIR detection is divided into 34

¹ <http://archive.spitzer.caltech.edu>, PID: 718

² IRAF is distributed by the National Optical Astronomy Observatories, which are operated by the Association of Universities for Research in Astronomy, Inc., under the cooperative agreement with the National Science Foundation

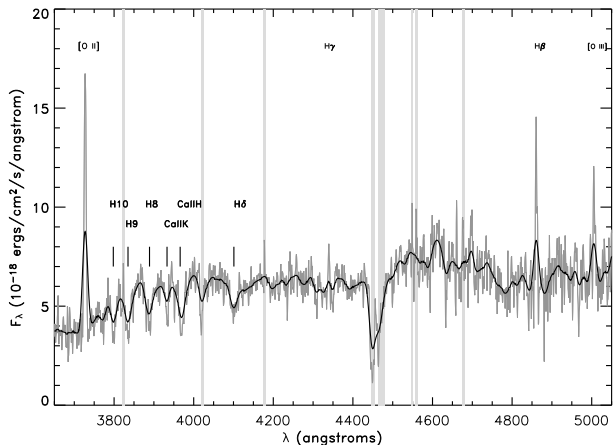


Fig. 2. Comparison of the VLT-FORS2 raw spectrum (grey line) of the distant LIRG UDSR23 ($z=0.7094$, $51.8 M_{\odot} \text{ yr}^{-1}$) to its wavelet decomposition resulting from the combination of the four wavelet scales 4-7, i.e. from 11.2 to 89.6 \AA (black line). While the absorption lines are clearly distinguishable, the emission lines such as [OIII],[OII],H β ,H γ are partly diluted by this technique.

”normal” galaxies, 36 LIRGs and 6 ULIRGs, where ”normal” galaxies consist in all galaxies except IR luminous galaxies (i.e. LIRGs and ULIRGs). The median SFRs associated to each total IR luminosity bin are 4, 54 and $196 M_{\odot} \text{ yr}^{-1}$ respectively. Because good quality spectra are required to study the stellar absorption lines ($S/N > 3$ on the continuum per resolution element), the final sample that we study in the present paper consists of 25 LIRGs with IR luminosities ranging between 10^{11} and $10^{12} L_{\odot}$. The median redshift of the final sample is $\bar{z}=0.7$. The measured properties of the galaxies are summarized in Table 1.

The total (8-1000 μm) IR luminosities, L_{IR} , were derived using the library of template SEDs built by Chary & Elbaz (2001), as in Elbaz et al. (2005). We also computed L_{IR} from the Dale & Helou (2001) library following the technique described in Marcillac et al. (2005) and found a median value for L_{IR} 10 % lower than with the previous library and with an rms of 17 %, hence both techniques provide consistent luminosities. We then compared the L_{IR} derived with 15 μm and/or 24 μm flux densities for the 11 galaxies detected with both ISOCAM and MIPS. Both libraries of template SEDs provide consistent determinations of L_{IR} using both measurements (with an rms of 30 %, see also Elbaz et al. 2005). The median L_{IR} derived from MIPS is 10 % lower than the one derived from ISOCAM using both libraries which suggests a possible variation of the MIR spectra of LIRGs as a function of redshift (see Marcillac et al. 2005).

2.2. Observations and data reduction

The observations were performed during three nights with FORS2 on the ESO-VLT with the combination of the grisms R600 and I600 (3 hours per grism) to cover the wavelength

wavelet scale	resolution (\AA)
0	0.7
1	1.4
2	2.8
3	5.6
4	11.2
5	22.4
6	44.8
7	89.6

Table 2. Definition of the wavelet scales used in the wavelet decomposition of the VLT-FORS2 spectra. The spectral resolution is equal to the highest resolution of $0.7 \times 2^{\text{wavelet scale}} \text{ \AA}$. See description in the text for the construction of the different wavelet transforms at each scale.

range 5000 to 9200 \AA at a resolution of 5 \AA ($R=1200$). At the median redshift of the objects of $\bar{z} \sim 0.7$, the resolution is equivalent to 3 \AA ($R=2000$).

Because absorption lines are wider than emission lines, it is possible to increase the signal-to-noise ratio on the absorption lines by working at a lower frequency than the raw spectrum. The physical origin of the width of the absorption lines results from the complex combination of the internal dynamics of the stars and the global dynamics of the galaxy. In order to optimize the line extraction, we therefore decomposed the raw spectra into eight different wavelet scales (Table 2) using the undecimated (keeping an identical sampling in each wavelet scale) wavelet transform (à trous algorithm; Starck & Murtagh 1994, Starck, Pantin & Murtagh 2002). We optimized the S/N ratio on the absorption line features by selecting the best combination of wavelet scales. In the wavelet space, the first scale (highest frequency), that we index as scale 0, corresponds to features of size 0.7 \AA , while features at scale j have a size of $0.7 \times 2^j \text{ \AA}$. Note that the lowest frequency scale is equivalent to the raw spectrum smoothed by a B-spline (equivalent to a gaussian) of width 89.5 \AA , i.e. the baseline, while at higher frequencies, each wavelet scale ‘i’ is equal to the difference between the raw spectrum smoothed at the scales ‘i’ and ‘i-1’. Hence the sum of all wavelet scales plus the baseline (here at scale 7) is exactly equal to the initial raw spectrum.

In order to determine the number of scales to take into account in the decomposition, we started from the lowest resolution in the wavelet space, equivalent to a spectral resolution of 89.5 \AA . We then kept doubling the frequency level as long as the S/N ratio was increased. This happened at the wavelet scale ‘4’ (equivalent to 11.2 \AA), hence we used the co-addition of the 4,5,6 and 7 wavelet scales (from 11.2 to 89.6 \AA , increasing the frequency by a factor 2 for each scale) in order to reconstruct spectra devoid of high resolution noise. The steps of the decomposition are shown in the Fig 1 for a LIRG, UDSR23 ($z=0.7094$), located at the median redshift of the sample. The spectra resulting from the combination of these four scales present the advantage of seeing the same spectral resolution as the one used by Bica & Alloin (1986). The final result is compared to the raw spectrum in the Fig. 2.

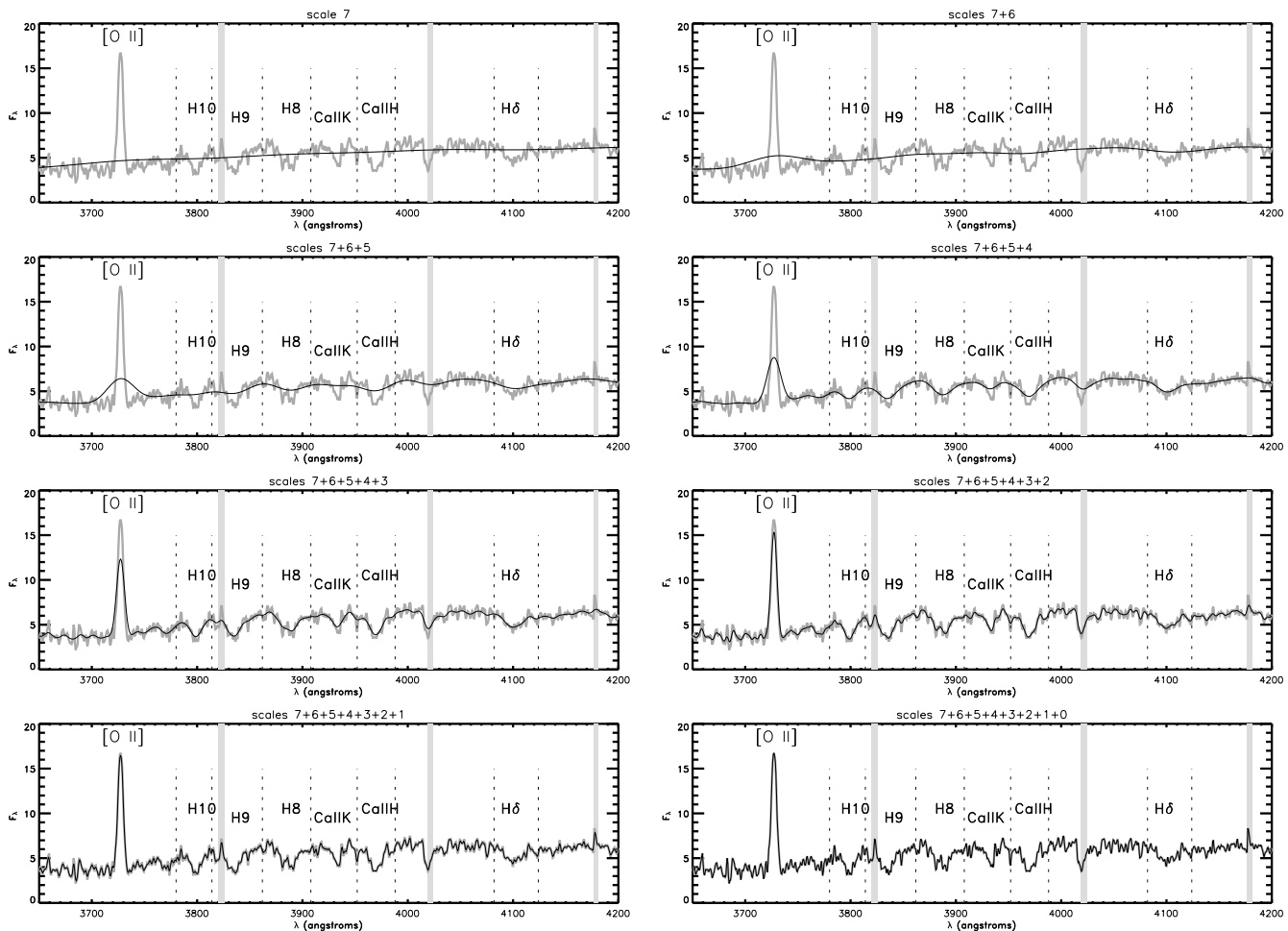


Fig. 1. Wavelet decomposition of the VLT-FORS2 spectrum of a distant LIRG (UDSR23) located at a redshift of $z=0.7094$ and forming stars at a rate of $\text{SFR}_{\text{IR}} = 51.8 \text{ M}_{\odot} \text{ yr}^{-1}$. The raw spectrum (thick grey line) is compared to its wavelet decomposition (thin dark line), starting from scale 7, corresponding to the spectrum smoothed with a B-spline (equivalent to a gaussian) at the lowest resolution of 89.6 \AA , then adding up the wavelet scales by increasing the spectral resolution from 44.8 \AA (scale 6) to 0.7 \AA (scale 1), by dividing it by a factor 2 for each scale. The narrow vertical grey zones were masked in the analysis because of the presence of sky emission lines. The vertical dotted lines indicate the minimum and maximum wavelength for each absorption line. In this zoom, the absorption lines clearly appear as much shallower than the emission line in OII.

Note that the wavelet decomposition can dilute emission lines and that we have checked that absorption lines were not affected by a similar effect. Being wider, they are naturally less affected by this technique. However, we quantified this effect using some stellar spectra extracted from STELIB (Le Borgne et al 2003) which resolution is about the same as the rest-frame one for the distant LIRGs. We added a white noise to the stellar spectra to reach a signal to noise ratio of $S/N \sim 3$ on the continuum, interpolated the spectra to reach a resolution of 0.7 \AA and applied to them the same wavelet decomposition as for the distant LIRGs. The equivalent widths of the Balmer absorption lines determined before and after the wavelet analysis differ by less than 4%. We included this weak difference in the equivalent width uncertainties.

2.3. Measurement of the Balmer absorption line indices and 4000 Å break

In the following, we will compare the equivalent widths measured for $H\delta$ (4101 \AA) and for the high-order Balmer absorption line H8 (3889 \AA). We also considered using the H9 (3835 \AA) line that we therefore also define in this section, but it appeared to be a less reliable tracer of the past star formation activity of galaxies, as we discuss in the next section.

We used the definition of the $H\delta$ pseudo-equivalent width indice as defined in the Lick system (Worthey & Ottaviani 1997) (see table 3). Since no Lick indices have yet been defined for the high order Balmer absorption lines, we adapted the windows defined by Bica & Alloin (1986) to the Lick index method for H8 and H9: for each line, the index continuum, the blue and red bandpasses for each pseudo-continuum are summarized in table 3. The two latter lines present the advantage of being located at a lower wavelength, to be accessible to higher

Name	Blue and red bandpasses (Å)	Index continua(Å)
$H\delta_A$	4041.60-4079.75 4128.50-4161.00	4083.50-4122.25
H9	3810-3820 3855-3865	3825-3845
H8	3855-3865 3905-3915	3870-3900

Table 3. Definition of the pseudo-equivalent width indices for the $H\delta$ ($H\delta_A$ in Worthey & Ottaviani 1997) and for the two high order Balmer absorption lines. For the two last lines, we followed the same principle as for Lick indices while using windows defined Bica & Alloin (1986).

redshifts in the observed optical range and to be less affected by the overlying nebular emission lines at the same wavelengths.

The $H\delta$ absorption line is surrounded by iron absorption lines which affect both its red and blue pseudo continua and are responsible for the negative EW measured for this line after a few Gyears, as discussed in the next section. In order to avoid such pollution from neighbouring lines, the red continuum of H8 was chosen to minimize the sensitivity to the CaII H (3933 Å) and K (3966 Å) lines while the 3855-3865 Å region is not known to be affected by metallic lines. As a result this index is weakly affected by metallicity. H9 is the least polluted line because no metallic line is located near it, but it is somewhat fainter than H8 and it is surrounded by the strong absorption of H8 and H10 which makes the two pseudo continua more difficult to define. We have primarily used $H\delta_A$ and H8, which are better determined for most of our spectra but also checked that we obtained consistent results based on the H9 and $H\delta$ lines when they were available. Note that we will discuss separately the results obtained with the Balmer absorption lines $H\delta_A$ (4102 Å) and H8 (3889 Å). The advantage of this choice is that it provides two independent estimates of the parameters that we are deriving and can be used as a test of the robustness of the Bruzual & Charlot (2003) code that we are using.

Note also that there is an ongoing debate about the possible misinterpretation of the equivalent width of the $H\delta_A$ line because of metallicity ratios which could affect its neighboring regions, hence its associated pseudo-continua (see Thomas *et al.*, 2004, Korn *et al.*, 2005). On the one hand, $H\delta_A$ presents the advantage to allow the comparison with studies of local galaxies such as SDSS galaxies (Kauffmann *et al.* 2003) while H8 is usually not available for local galaxies because it lies in a bluer region of the spectrum. On the other hand, the H8 line is not known to be affected by neighboring metallic lines and as it is located in a bluer region of the spectrum, it is easier to measure for distant galaxies (less polluted by sky emission lines).

Before measuring these absorption features, we have corrected them from the overlying nebular emission line whenever possible as indicated in the paper. The nebular emission lines are not detected directly from the spectra, because they are too faint, but we computed their emission based on the observed H_β and H_γ emission lines (and H_α for the low- z galaxies) assuming a line ratio corresponding to a case B recombination for electron densities $\leq 10^4 \text{ cm}^{-3}$ and temperatures $T_e \sim 10^4$ (Osterbrock, 1989). The Balmer emission line ratio was also used to compute the attenuation of these lines before subtract-

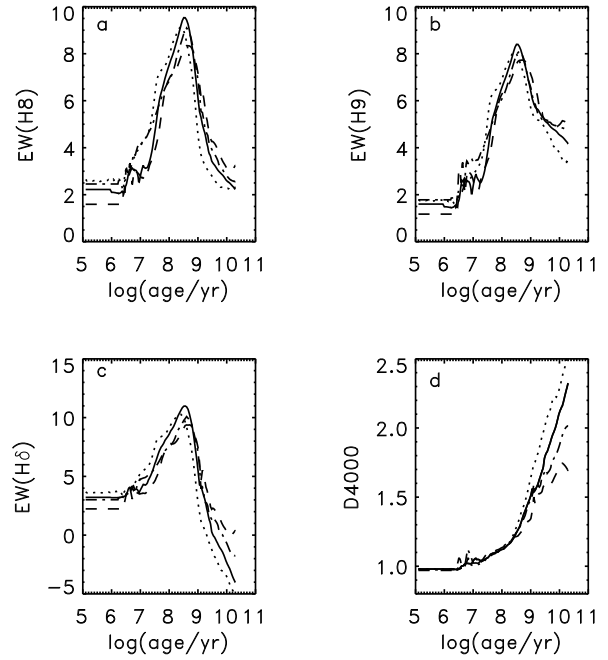


Fig. 3. Time evolution of the H8, H9 and $H\delta_A$ indices and 4000 Å break (D4000) for a single stellar population synthesized with the GALAXEV code (Bruzual & Charlot 2003). Four different metallicities were used in each plot demonstrating the marginal effect of metallicity on the three indices and on D4000 before 1 Gyr: $Z=0.004$ (20% solar, dashed line), $Z=0.008$ (40% solar, dash-dotted line), $Z=0.02$ (solar, solid line), $Z=0.05$ (2.5 times solar, dotted line). From top to bottom and left to right: a) H8 evolution, b) H9 evolution, c) $H\delta_A$ evolution, d) D4000 evolution.

ing them from the absorption lines measurements. The computation and values for these attenuations can be found in Paper I.

Following the same strategy as Kauffmann *et al.* (2003), we used the method explained in Bruzual (1983) and the blue and red bandpass definitions introduced by Balogh *et al.* (1999). The latter are narrower than the ones originally defined by Bruzual (1983) and present the advantage of being less sensitive to reddening effects.

H8 and D4000 values for each distant LIRG are summarized in Table 1. The scientific interpretation is discussed in the following section.

3. 4000 Å break and Balmer absorption lines as tracers of the recent star formation history

In this section, we describe how Balmer absorption lines and the 4000 Å break trace the recent star formation history of galaxies. For this purpose, we have synthesized a single stellar population (SSP) using the latest version of the 'GALAXEV' code from Bruzual & Charlot (2003). For the moment, we do not include dust attenuation to simplify the discussion. Note however that the wavelength range over which the equivalent widths and the 4000 Å break are measured is small

which implies a marginal correction due to dust attenuation. Nonetheless, we will include dust attenuation in the Monte Carlo realizations that we will compare to the LIRGs and discuss its effects on our findings.

This version of the GALAXEV code includes the spectral library STELIB (Le Borgne et al. 2003) whose spectral resolution is 3\AA from 3200 to 9500\AA , which is comparable to the present spectra in the rest-frame of the galaxies. Fig. 3 presents the evolution with time of the high order Balmer absorption lines H8 and H9 as well as the $H\delta_A$ absorption line and the 4000\AA break. The four lines in each plot correspond to four different metallicities with the following metal mass fractions (total mass in elements heavier than hydrogen and helium over the mass in hydrogen): $Z=0.004$ (20% solar, dashed line), $Z=0.008$ (40% solar, dash-dotted line), $Z=0.02$ (solar, solid line), $Z=0.05$ (2.5 times solar, dotted line).

The D4000 is the sudden onset of stellar photospheric opacity shortward of 4000\AA . It reflects the mean temperature of the stars responsible for the continuum: the metals located in the atmosphere of O and B stars are more ionized and produce a weaker opacity, hence a smaller 4000\AA break, than those in cooler stars (Bruzual 1983, Poggianti & Barbaro 1997, Gorgas et al 1999, Kauffmann et al 2003). Hence D4000 keeps increasing as a function of the aging of the stellar population (see Fig. 3d). D4000 is sensitive to metallicity as it is shown in tab. 3d where it varies by more than 20% after a few billion years, or when it is larger than 1.6. As we will see in the next section, the distant LIRGs have $D4000=1.2\pm 0.07$, and therefore for them metallicity effects are negligible. Even if the slope of D4000 versus age is less flat than for young population, i.e. 7 Gyears, it is flat enough to provide uncertain stellar ages if used alone.

In order to trace back the recent star formation history of galaxies, it is therefore necessary to use another tracer of stellar age such as the Balmer absorption lines, which exhibit a steep slope as a function of stellar ages in this range of ages (see Figs. 3a,b,c). Balmer absorption lines are dominantly produced by the atmosphere of A to F stars. However O and B stars, which do not exhibit strong absorption lines, indirectly affect them by increasing the continuum level and therefore diluting them, which explains the flat values for the equivalent widths of H8, H9 and $H\delta_A$ in the first few millions years (lifetime of O and B stars). The rapid increase that follows is produced by the dominant role of A and F stars, which then disappears after ~ 0.5 Gyr producing the rapid decline of the equivalent widths in Fig. 3a, b and c. Here again, it is worthwhile noticing the marginal role played by the metallicity on the evolution of the Balmer lines EW with time. The EW varies by less than 20% a few billion years after the burst as a function of metallicity.

4. Comparison of local and distant LIRGs

A sample of 401 local ($z \leq 0.25$) LIRGs detected with IRAS, with optical spectra from the SDSS and emission lines typical of star forming galaxies, as opposed to AGNs, was identified by Pasquali et al. (2005). The locus of the D4000 and EW ($H\delta_A$) measured for the distant LIRGs (green filled circles) is compared to that of local LIRGs (blue triangles) and of the field

indice	distant LIRGs	local LIRGs
D4000	$1.2^{+0.07}_{-0.07}$	$1.25^{+0.12}_{-0.08}$
$H\delta_A$	$5.0^{+1.5}_{-1.1}$	$4.9^{+1.07}_{-1.5}$

Table 4. Median and 68% dispersion (around the median) of the D4000 and $H\delta_A$ indices for local and distant galaxies.

SDSS galaxies (black dots) in Fig. 4. First, note the concentration of both LIRG populations at low D4000 and high $H\delta_A$, which suggests that local and distant LIRGs share a similar recent star formation history. We could not produce similar figures for high order Balmer absorption lines for this comparison since they are too blue to be accessible in the SDSS spectra. Their position in the D4000- $H\delta_A$ diagram indicates that the young stellar population that is producing the large IR luminosity is not completely obscured by dust in the optical because the median D4000 value of 1.2 for these galaxies correspond to stellar ages lower than 1 Gyr, which is much below the ages of these galaxies (see Table 4). This already suggests that even in these dusty galaxies the optical spectral signatures can be used as a tracer of the recent star formation history. The quasi absence of distant LIRGs above $D4000=1.25$, where half of the local LIRGs lie, suggests that the distant LIRGs are younger than the local ones.

The relative proportion of young and old stellar populations can be studied in these galaxies by comparing the stellar masses, derived mostly from the old stellar population dominating in the near infrared range, with their D4000 values. Massive galaxies are generally older as shown by Fig. 5, where the stellar mass of SDSS galaxies (black dots) increases with D4000. The position of the local LIRGs (orange filled dots) in Fig. 5 suggests that they are massive galaxies which were located on the right side of the plot before the burst and which were shifted to the left during the burst, which decreased their D4000 value. This figure reinforces our interpretation that the low value of D4000 for the LIRGs is due to the addition of a young population on top of an older population. The comparison of field SDSS galaxies with IRAS LIRGs in four bins of D4000 from 1 to 1.4 (bin size 0.1, 68% error bars) shows that local LIRGs exhibit systematically lower D4000 values for their stellar masses.

The incompleteness of the photometric data for our sample of galaxies prevented the determination of their stellar masses. However, another sample of mid IR selected LIRGs at $\bar{z} = 0.7$ located in the Hubble Deep Field South was studied by Franceschini et al. (2003) who computed their stellar masses using a Salpeter IMF and a combination of single stellar populations with ten different ages, to fit their UV-optical-NIR spectra of IR luminous galaxies. From their Table 6, a total of 14 LIRGs possess a spectroscopic redshift between $z=0.4$ and 1.2, and 7 more have a photometric redshift in this range. After converting Franceschini's values to $H_0=75\text{ km s}^{-1}\text{ Mpc}^{-1}$, we find a median stellar mass of $7\times 10^{10} M_\odot$ for the 14 galaxies with a spectroscopic redshift. Including the less robust photometric redshifts only changes this value to $6\times 10^{10} M_\odot$. Combined with a median $D4000\sim 1.2$, this places the distant LIRGs in a

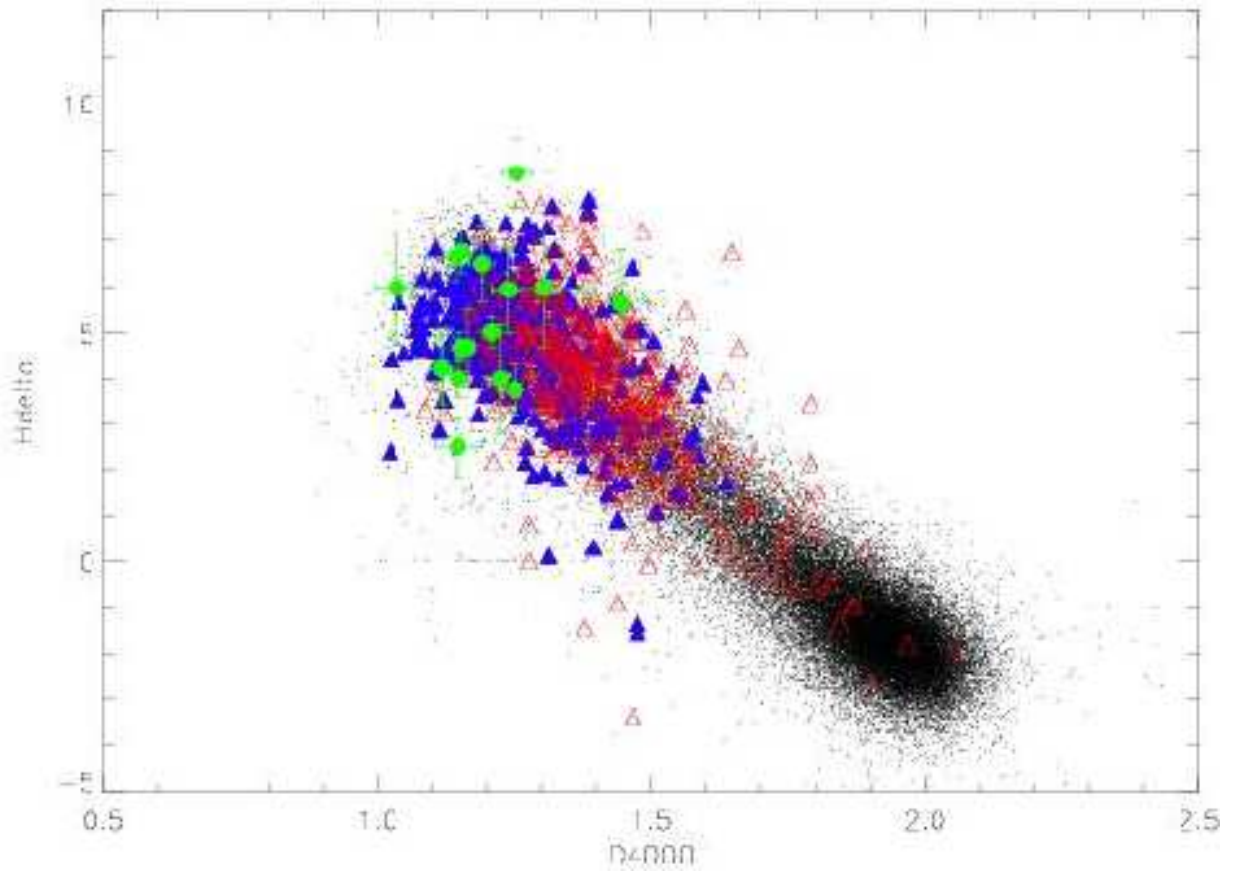


Fig. 4. $H\delta_A$ versus $D4000$ diagram for the SDSS galaxies (black points) and distant LIRGs of the present sample (green filled circles with error bars). The sub-population of SDSS galaxies detected with IRAS are marked with triangles and separated into galaxies with optical spectra with (empty red triangles) and without (filled blue triangles) an AGN signature.

very similar locus as the local LIRGs (see Fig. 5). Their low $D4000$ values are therefore also representative of the young stellar population of the burst superimposed on top of an older stellar population dominating the stellar mass of the galaxies.

5. Description of the model

We used the Bruzual & Charlot (2003) model to synthesize a series of 200,000 Monte Carlo realizations including various star formation histories. Although the technique is similar to the one used in Kauffmann et al. (2003), it presents two differ-

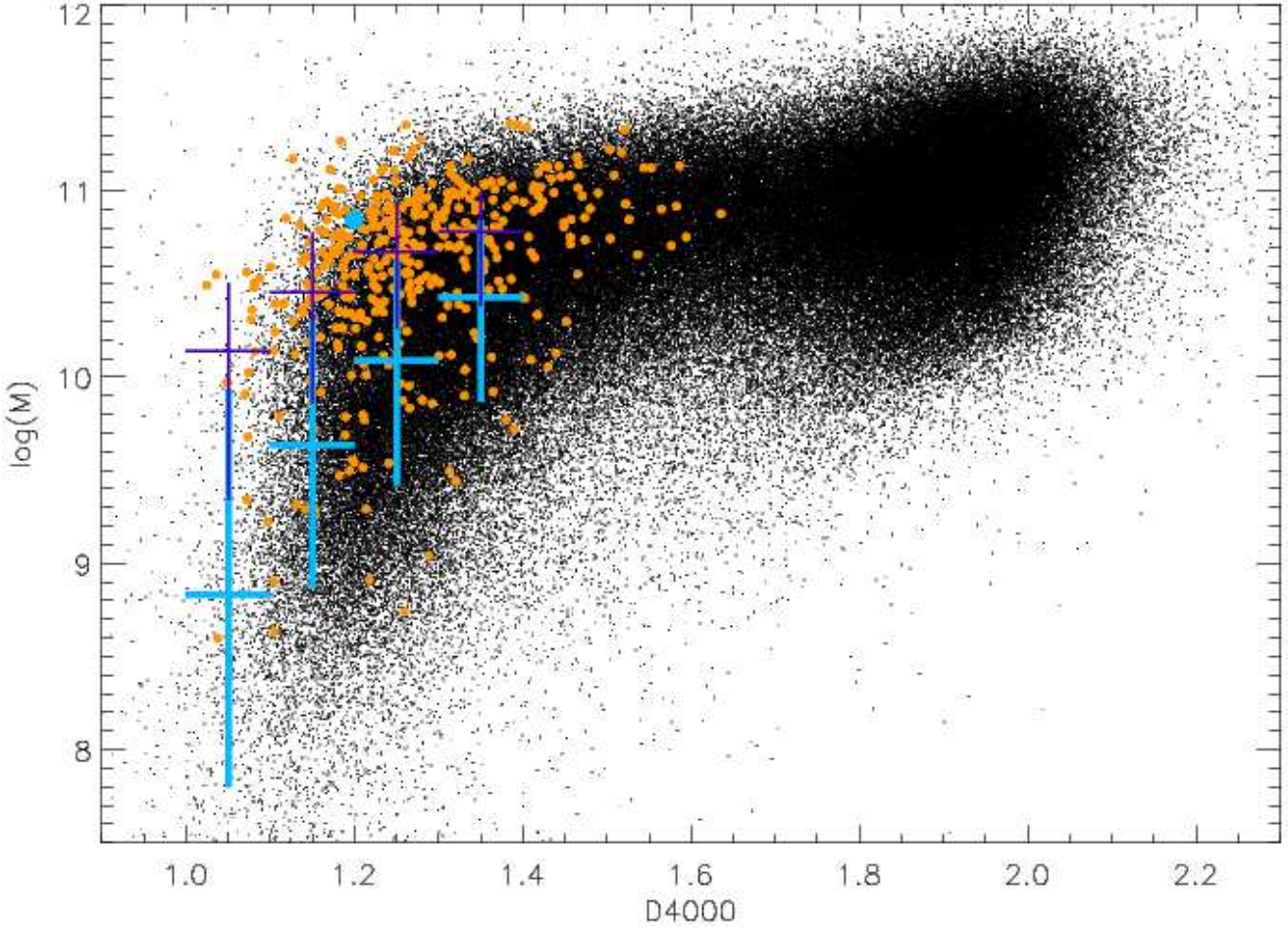


Fig. 5. Stellar mass as a function of D4000 for the SDSS galaxies (black points) and distant LIRGs of the present sample (large filled blue circle). The median stellar mass for the distant LIRGs was derived from Franceschini et al. (2003) as discussed in the text. The sub-population of SDSS galaxies detected with IRAS and without an AGN signature in their optical spectra (star forming galaxies) are marked with orange filled circles. The median and $1\text{-}\sigma$ error bars for the field SDSS galaxies are represented with thick light-blue crosses, while the thin dark-blue crosses are for the sub-sample of star forming SDSS-IRAS galaxies.

Continuous star formation	
t_{form} (Gyr)	1–7
γ (Gyr^{-1})	0–3
Metallicity & velocity dispersion	
Z/Z_{\odot}	0.5–1.5
V_{disp} (km.s^{-1})	100–300
Attenuation	
τ_V	1–4
μ	0.1–1.0
Burst fraction and duration	
f_B	0–1
τ_B (10^8 yr)	0.1–10

Table 5. Description of the range of values used as priors for the simulations.

ences related to the populations of galaxies that we are studying here, i.e. dusty starbursts. The priors of the model were set to include a range of dust attenuations and to include a larger frac-

tion of starbursting galaxies. We will discuss the effects of both modifications in the following.

Each star formation history was modeled with eight parameters:

- the age of the galaxy since its formation, t_{form} . We imposed a maximum age of 7 Gyr, which is the age of the universe at the median redshift of the galaxies, $\bar{z} \sim 0.7$.

- the parameter γ for the underlying "continuous" SFR (as opposed to the starburst itself): $\text{SFR}^{\text{cont}}(t) \propto e^{-\gamma t}$

- the SFR of the burst itself, $\text{SFR}^{\text{burst}}$, is not a parameter but results from the combination of two parameters: the burst duration, τ_B , and the stellar mass fraction produced during the burst, f_B . Note that f_B computed in the model is the ratio of the stellar mass formed during the burst, M_{\star}^{burst} , over the total stellar mass formed through continuous star formation during t_{form} , M_{\star}^{cont} . Here M_{\star}^{cont} is not corrected for the mass returned to the interstellar medium by evolved stars and is therefore larger than the actual stellar mass of the galaxy, M_{\star} . In the following, we will call, f_B^{eff} , the "effective burst stellar mass fraction", computed with M_{\star} instead of M_{\star}^{cont} .

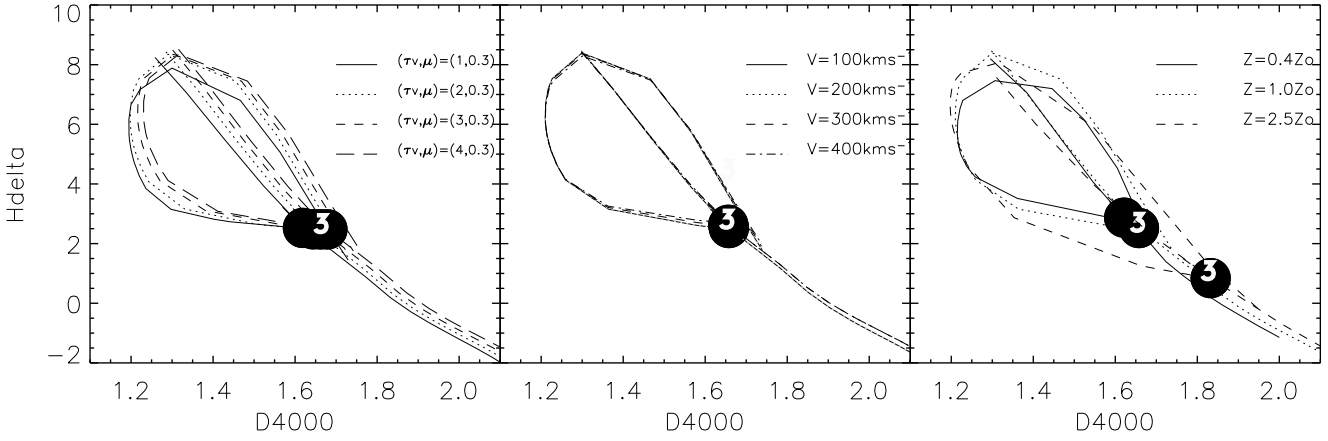


Fig. 6. Influence of the attenuation, velocity dispersion and metallicity for a typical star formation history synthesized with the GALAXEV code (Bruzual & Charlot, 2003). In all three plots, the loops correspond to a burst of star formation which started 3 Gyr (big black circles) after the galaxy’s birth. **a) Influence of the attenuation** τ_v : for a continuous star formation ($\gamma=1.0$, $V_{\text{disp}}=200\text{km.s}^{-1}$, $\mu=0.3$, $Z=Z_{\odot}$) and a single burst ($\tau_B=0.1$ Gyear and $f_B=10\%$); the solid line : $\tau_v=1.0$. The dotted line : $\tau_v=2.0$. The dashed line : $\tau_v=3.0$. The long dashed line : $\tau_v=4.0$. **b) Influence of the velocity dispersion** V_{disp} : for a continuous star formation ($\gamma=1.0$, $\tau_v=3.0$, $\mu=0.3$, $Z=Z_{\odot}$) and a single burst ($\tau_B=0.1$ Gyear and $f_B=10\%$). The solid line : $V_{\text{disp}}=100\text{ km.s}^{-1}$. The dotted line : $V_{\text{disp}}=200\text{km.s}^{-1}$. The dashed line : $V_{\text{disp}}=300\text{ km.s}^{-1}$. **c) Influence of the metallicity** Z : for a continuous star formation ($\gamma=1.0$, $V_{\text{disp}}=200\text{km.s}^{-1}$, $\tau_v=3.0$ and $\mu=0.3$) and a single burst ($\tau_B=0.1$ Gyear and $f_B=10\%$). The solid line : $Z=0.5Z_{\odot}$. The dotted line : $Z=Z_{\odot}$. The dashed line : $Z=2.5Z_{\odot}$.

- the dust attenuation parameters, μ and τ_v , defined as in Charlot & Fall (2000), i.e. a differential attenuation function of the age of the stars (see Eq. 1 and Fig. 6a). Stars younger than 10^7 years, the typical lifetime of a giant molecular cloud (GMC), are assumed to be embedded in their dusty parent GMC with an optical depth τ_v . Older stars are supposed to have escaped their parent GMC and their ambient medium’s optical depth is assumed to be μ times smaller. This attenuation law was chosen because it reproduces well the correlation observed for UV selected starbursts of the FIR over UV ratio with the UV slope, β , as well as the $L_{\text{H}\alpha}$ over $L_{\text{H}\beta}$ ratio. The optical depth for stars younger than 0.1 Gyears, τ_v , was set between 1 and 4 based on the observed values for LIRGs (Liang *et al.* 2004, Flores *et al.*, 2004), while μ was allowed to vary from 0.1 to 1.

$$\begin{aligned}
 F_{\lambda}^{\text{observed}} &= F_{\lambda}^{\text{intrinsic}} \times e^{-\tau_{\lambda}} \\
 \tau_{\lambda} &= \tau_v \times (5500/\lambda)^{0.7} & t_{\star} < 10^7 \text{ yr} \\
 \tau_{\lambda} &= \mu \times \tau_v \times (5500/\lambda)^{0.7} & t_{\star} \geq 10^7 \text{ yr}
 \end{aligned} \quad (1)$$

- the velocity dispersion, V_{disp} . We allowed a large range of velocity dispersions to test the effect of a broadening of the $\text{H}\delta_A$ absorption lines that would mimick intrinsically large width of the absorption lines due to the combination of the internal dynamics of the stars with the mass of the galaxy. The influence of the velocity dispersion on the position of a galaxy in the $\text{H}\delta_A$ -D4000 diagram was found to be negligible (see Fig. 6b).

- the metallicity, Z . The influence of the stellar metallicity is stronger than that of the velocity dispersion but remains smaller than the error bars on the measured $\text{H}\delta$ and D4000 (see Fig. 6c).

Table 5 summarizes the range over which those eight parameters were chosen, the so-called priors, which represent the key adjustment when using a Bayesian statistics. The goal of

these simulations is not to constrain all eight parameters and indeed some of them produce competitive effects or cannot be disentangled:

- a galaxy with a given age and γ parameter for its SFR will be located at the same position in the $\text{H}8$ -D4000 diagram than a younger galaxy with a larger value for γ .

- the two parameters used in the attenuation law, μ and τ_v . Fig. 6 shows that galaxies are shifted towards the upper-right of the $\text{H}\delta_A$ -D4000 (or equivalently $\text{H}8$ -D4000) diagram with increasing dust attenuation. This is an important point to note when comparing dusty galaxies to field galaxies: even though LIRGs overlap with a fraction of SDSS field galaxies in the Fig. 4, their recent star formation history is interpreted differently if their dust attenuation is taken into account.

Instead, we will use a bayesian approach such as the one detailed in Kauffmann *et al.* (2003) to derive the following characteristics of the starbursts:

1. the Scalo parameter, i.e. the ratio of present to past-averaged star formation rate. This parameter defines the relative intensity of the present starburst.
2. the burst duration, τ_B .
3. the last burst stellar mass fraction, f_B (and f_B^{eff}).

The bayesian statistics approach consists in determining a probability distribution function (PDF) for any one of these parameters, which consists in an histogram of the number of Monte Carlo realizations weighted by the probability function $\exp(-\chi^2/2)$, where χ^2 is defined in Eq. 2. The convergence of the technique is reached if the PDF is peaked and its shape provides the precision of the determination.

$$\chi^2 = \left(\frac{\text{H}\delta^{\text{obs}} - \text{H}\delta^{\text{sim}}}{\sigma(\text{H}\delta^{\text{obs}})} \right)^2 + \left(\frac{\text{D4000}^{\text{obs}} - \text{D4000}^{\text{sim}}}{\sigma(\text{D4000}^{\text{obs}})} \right)^2 \quad (2)$$

6. Results

6.1. Signature of the presence of a starburst in the distant LIRGs in the H8-D4000 diagram

We generated three series of simulations with the same priors but varying the percentage of galaxies experiencing a starburst at the age of the simulated spectrum. In a first simulation, SIM1, only 20 % of the Monte Carlo realizations include ongoing starburst. The positions in the H8-D4000 diagram of the 200,000 Monte Carlo realizations of SIM1 are illustrated with small dots in Fig. 7. The light blue points on the lower-left part of the figure illustrate the position of galaxies with an ongoing burst of star formation. The upper dark blue points correspond to post-starbursts, i.e. galaxies having experienced a recent starburst which ended less than 2 Gyr ago, and dark points to galaxies with continuous star formation or at least no burst during the past 2 Gyears. The lines illustrate the tracks followed by an individual galaxy during its lifetime: a galaxy with purely continuous star formation will follow the bold red line, where the numbers mark its age in Gyr ($\gamma=2$, $\mu=0.3$, $\tau_V=3.0$, $V_{\text{disp}}=200 \text{ km.s}^{-1}$). If this galaxy was to experiment a burst of star formation when it is 3 Gyrs old, then it would follow one of the loops in light orange towards the left of the diagram for a total duration of 2 Gyrs and then go back to the track of a galaxy with pure continuous star formation, having lost the memory of its past starburst. During the loop, D4000 is at first the most affected by the presence of young stars, moving towards the left of the diagram, then it is H8 which increases moving upwards in the diagram, before the galaxy slowly goes back to the continuous regime. The first part of the loop is marked with small lines indicating that the galaxy is still bursting, while the remaining part of the loop corresponds to the post-starburst regime. We have plotted a loop starting at an age of 2 Gyears (light orange) and another starting at 3 Gyears (dark orange). In each case we computed the track of $\tau_B=5 \times 10^7$ years (dashed lines) and 10^8 years (plain line) starburst with a fraction of $f_B=15 \%$.

75 % of the distant LIRGs are located within the solid rectangle in Fig. 7, hence at the location of galaxies experiencing a starburst in the simulation. The remaining 25 % of the distant LIRGs lie in the dashed rectangle which includes the region of post-starbursts but also galaxies with successive or longer starbursts. Hence, the results of the simulation from SIM1 simulation show that the observed galaxies are mainly coherent with being starbursting galaxies.

As a second step, we designed a new simulation, with 80 % of the galaxies experiencing an ongoing starburst (SIM2), to better sample the locus of the distant LIRGs and therefore better study the properties of the starbursts themselves. A third and last simulation (SIM3) was generated to quantify the probability that the distant LIRGs experienced a previous starburst during the last 2 Gyr. Half of the galaxies in SIM3, i.e. 100,000 galaxies, have experienced a previous starburst during the last 2 Gyr, which ended before the onset of the ongoing starburst.

The individual positions of the distant LIRGs are compared to the SIM2 realizations in Fig. 8 and Fig 9 in the H8-D4000 and $H\delta_A$ -D4000 diagrams respectively. UDSR09, which is ly-

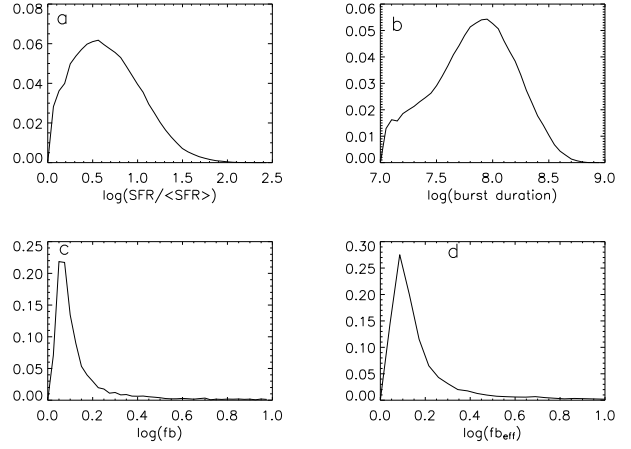


Fig. 10. Example of PDF obtained for 1 galaxy : a) The Scalo parameter (subsection 6.2). b) Burst duration (subsection 6.2). c) Burst fraction (subsection 6.2). d) Effective burst fraction (subsection 6.2).

ing at the bottom of the simulation is a clear outlier. Liang et al (2005) studied carefully this object and its optical spectrum shows strong metal absorption lines such as Ca H K, G-band, Mg H, Na D lines but weak Balmer absorption lines. The X-ray emission of this object, in addition is mainly associated to an AGN. As a consequence, an AGN can partially contribute to the MIR luminosity. Note that the observed galaxies are not identical in both figures neither in numbers nor in identity because both H8 and $H\delta_A$ cannot be both measured for all individual galaxies. The dots correspond to the same simulated galaxies in both figures and in both cases. Note that the observed LIRGs do lie below the continuous star formation regime in both figures, although in slightly different locations. These differences will be discussed in the subsection 6.5 when we will present the resulting PDFs. Note also that the distant LIRGs are distributed in two populations in Fig. 8, one located at the bottom of the diagram and a second at the upper-left. The second population corresponds to simulated galaxies which experienced a succession of two starbursts during the last 2 Gyrs. Such histories are expected in the framework of major mergers of spiral galaxies with several encounters between two galaxies.

6.2. Determination of the Scalo parameter, $SFR/\langle SFR \rangle$

The PDF obtained for the Scalo parameter of a typical galaxy with $SFR/\langle SFR \rangle \sim 2.7_{-1.0}^{+7.3}$ ($1-\sigma$) is represented in Fig. 10a. In about 60 % of the distant LIRGs, the PDF converge towards a determination of the Scalo parameter. For 10 out of 17 galaxies for $H\delta_A$ (see Table 6), we compute a median value of $SFR/\langle SFR \rangle = 3.0_{-0.6}^{+3.5}$ ($1-\sigma$). For 12 out of 22 for H8 (see Table 7) we find $SFR/\langle SFR \rangle = 4_{-1}^{+1}$ ($1-\sigma$). These two results are consistent with each other, as illustrated by the Figs. 11a and c. The fact that the H8-D4000 diagram provides the tightest constraint on the Scalo parameter is due to the fact that the sky background is lower in the bluer wavelength range of H8

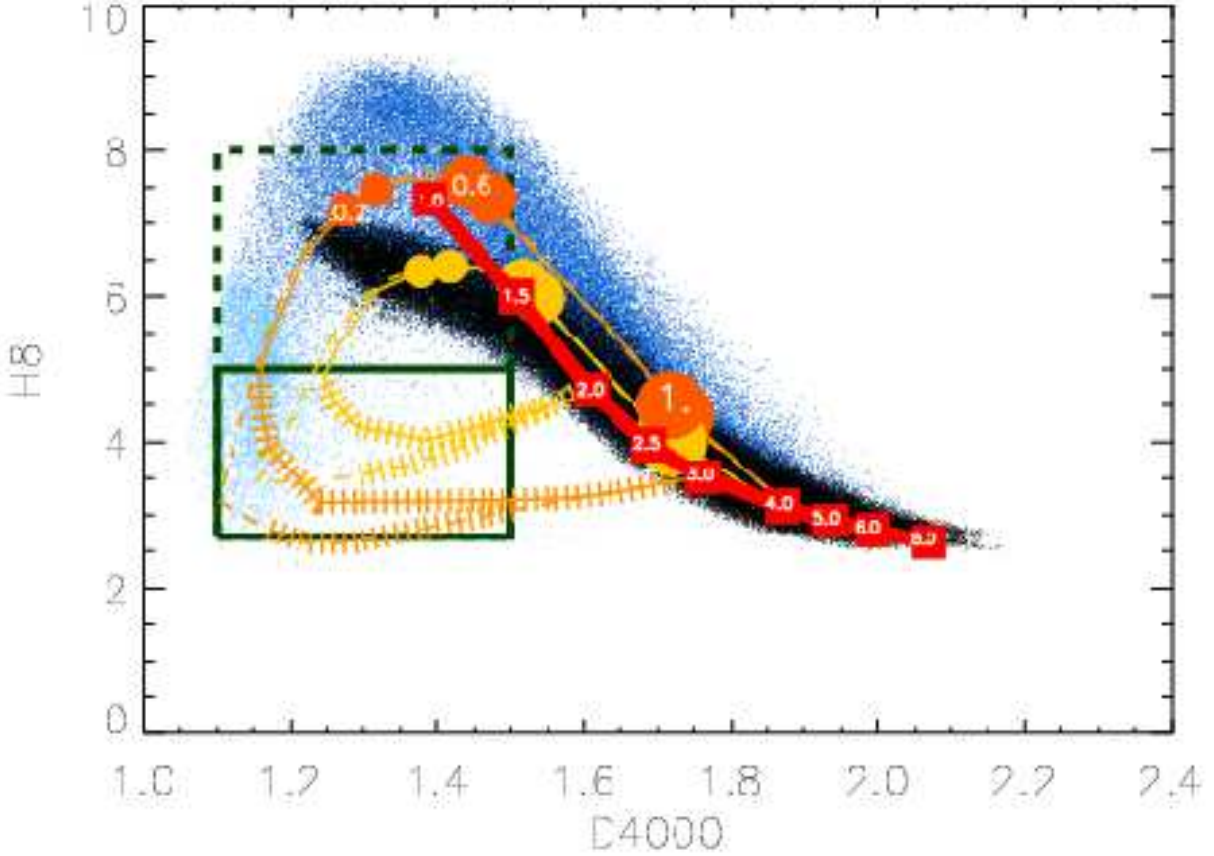


Fig. 7. Location of the 200,000 Monte Carlo realizations using the parameters of SIM1 (see table 5) in the H8 versus 4000 Å (D4000) break diagram. **Light blue points (lower-left):** starbursting galaxies. **Dark blue points (upper part):** post-starburst galaxies (galaxies having experienced a recent starburst which ended less than 2 Gyr ago). **Black points:** galaxies with a continuous star formation in the two past Gyears. **Bold red line:** track followed by an individual galaxy with continuous star formation (numbers in squares = age in Gyr) generated with GALAXEV ($\gamma=2.$, $\mu=0.3$, $\tau_V=3.0$, $V_{\text{disp}}=200 \text{ km.s}^{-1}$). **Orange loops:** effect of starbursts of 5×10^7 (dashed line) and 10^8 (plain line) years starting after 2 Gyr (light orange) and 3 Gyr (dark orange) of continuous star formation. The line is hatched during the starburst phase. The size of the orange dots is proportional to the time counted in 10^8 years units after the beginning of the burst. **The dark rectangle with dashed contours:** area where the distant LIRGs are located. **The dark rectangle with a solid line:** area where are lying 75 % of the sample (see Fig. 8 for the position of the individual galaxies with error bars). **Triangles:** galaxies corrected for the underlying nebular emission line in H8 as derived from the observed lower order Balmer lines corrected for attenuation from the Balmer lines ratio. **Stars:** galaxies with negligible emission Balmer line in emission, hence uncorrected for H8 emission. **Squares:** corrected for the underlying H8 emission line using only one Balmer emission line available with dust attenuation computed from the IR (from the ratio of $\text{SFR}(\text{IR})$ over $\text{SFR}(\text{H}\beta)$). **Circles:** no correction for the underlying potential emission line because no information is available on the Balmer emission lines.

than in $\text{H}\delta_A$. We will therefore use that range of values for the Scalo parameter in the next set of computations. The fact that the LIRGs are found to produce stars at a rate about four times larger than their averaged past SFR confirms that they are experiencing a major phase of star formation in their lifetime. This result is consistent with the large L_{IR} and $\text{SFR}(\text{IR})$.

As noted above, the H8-D4000 diagram provides the tightest constraint on the Scalo parameter with $\text{SFR}/\langle\text{SFR}\rangle = 4^{+1.0}_{-0.9}$. Combined with the ongoing SFR measured from the MIR emission for the distant LIRGs (quoted in Table 1) for indi-

vidual galaxies and with a median value of: $\overline{\text{SFR}} = 52^{+34}_{-33} \text{ M}_{\odot} \text{ yr}^{-1}$, the Scalo parameter allow us to compute the averaged past SFR of the distant LIRGs: $\langle\text{SFR}\rangle \sim 13 \pm 3 \text{ M}_{\odot} \text{ yr}^{-1}$.

If we assume that the progenitors of the distant LIRGs formed stars at a constant rate equal to the averaged past SFR, a median stellar mass of $7 \times 10^{10} \text{ M}_{\odot}$ (see Sect. 4) is assembled in about $5.5 \pm 1.5 \text{ Gyr}$ (light-weighted age), implying that the first dominant stellar populations formed at a redshift $z \sim 4.5 \pm 1.5$.

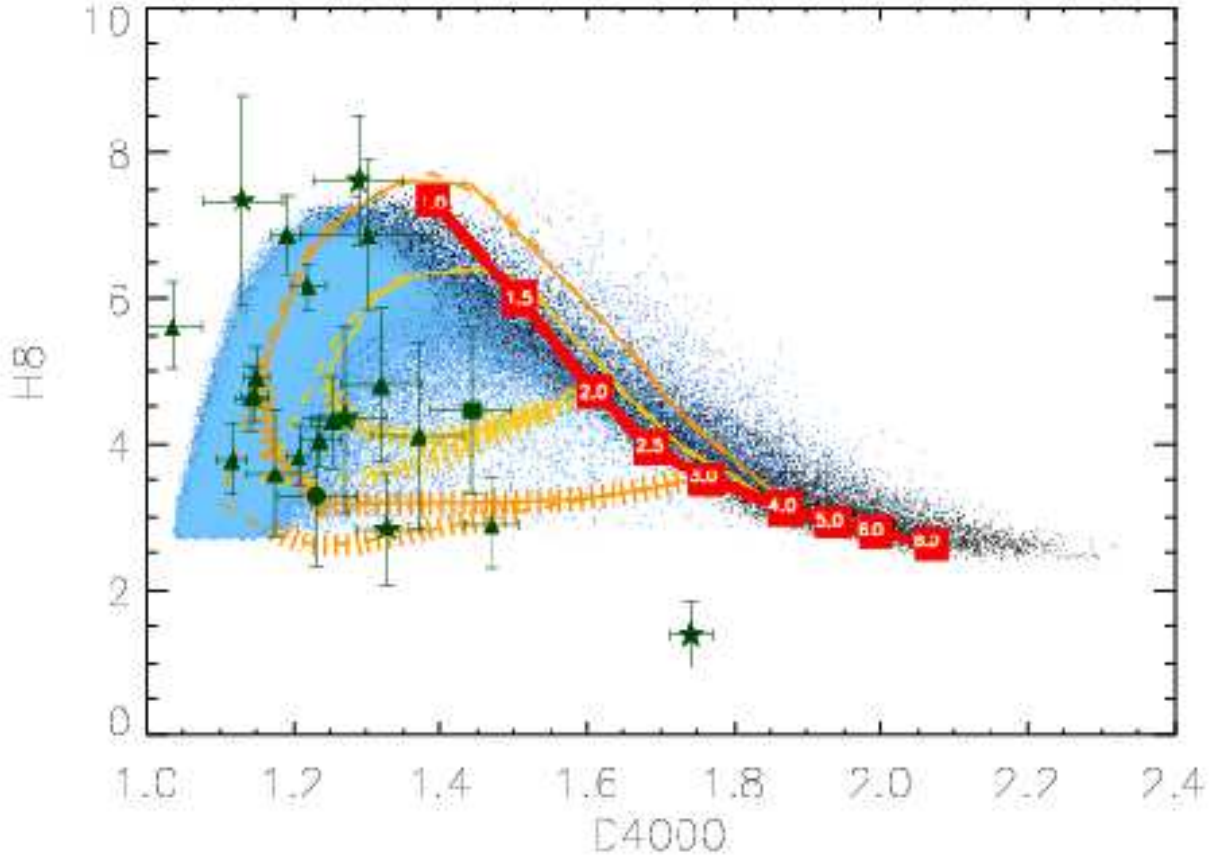


Fig. 8. Same as in Fig. 7 for the SIM2 Monte Carlo simulation of 200 000 model galaxies. The distant LIRGs are represented with green points with error bars.

id	SFR/<SFR> [68 %]	$(\tau_B) [(\tau_B^-, \tau_B^+)]$ $\times 0.1$ Gyr [68 %]	$f_B [f_B^-, f_B^+]$ (%) [68 %]	$f_B^{\text{cell}} [f_B^{\text{cell}-}, f_B^{\text{cell}+}]$ (%) [68 %]
UDSF07	6 [3, 24]	–	4 [3,17]	5 [3,25]
UDSF16	–	0.8 [0.3 , 3.0]	3[2,5]	4 [3,7]
UDSF17	2 [1, 5]	4 [1.5 , 6]	–	–
UDSF18	2 [1, 5]	1 [0.5 , 3]	4 [3,13]	5 [3,17]
UDSF19	–	1.6 [0.4 , 4.0]	2 [1,23]	3 [2,10]
UDSF31	–	–	–	–
UDSR08	6 [3, 27]	0.4 [0.2 , 1.3]	3 [2,16]	5 [3,26]
UDSR10	–	–	–	–
UDSR14	4 [2, 13]	0.3 [0.1 , 0.8]	4 [2,9]	5 [3,14]
UDSR20	–	5 [1 , 8]	–	–
UDSR23	3 [1, 10]	0.8 [0.3 , 1.6]	6 [4,9]	7 [5,19]
CFRS02	–	–	–	–
CFRS06	2 [1, 4]	2. [1 , 4]	2 [1,9]	7 [5,19]
CFRS08	–	–	–	–
CFRS10	10 [5, 36]	1 [0.2 , 2.0]	13 [7,30]	14 [7,47]
CFRS11	3 [2, 15]	–	3 [2,5]	4 [3,9]
CFRS14	3 [2, 6]	3 [1 , 6]	–	–

Table 6. Results concerning the burst duration, the Scalo ratio SFR/<SFR>, and the burst fraction (f_B) when using the $H\delta_A$ data.

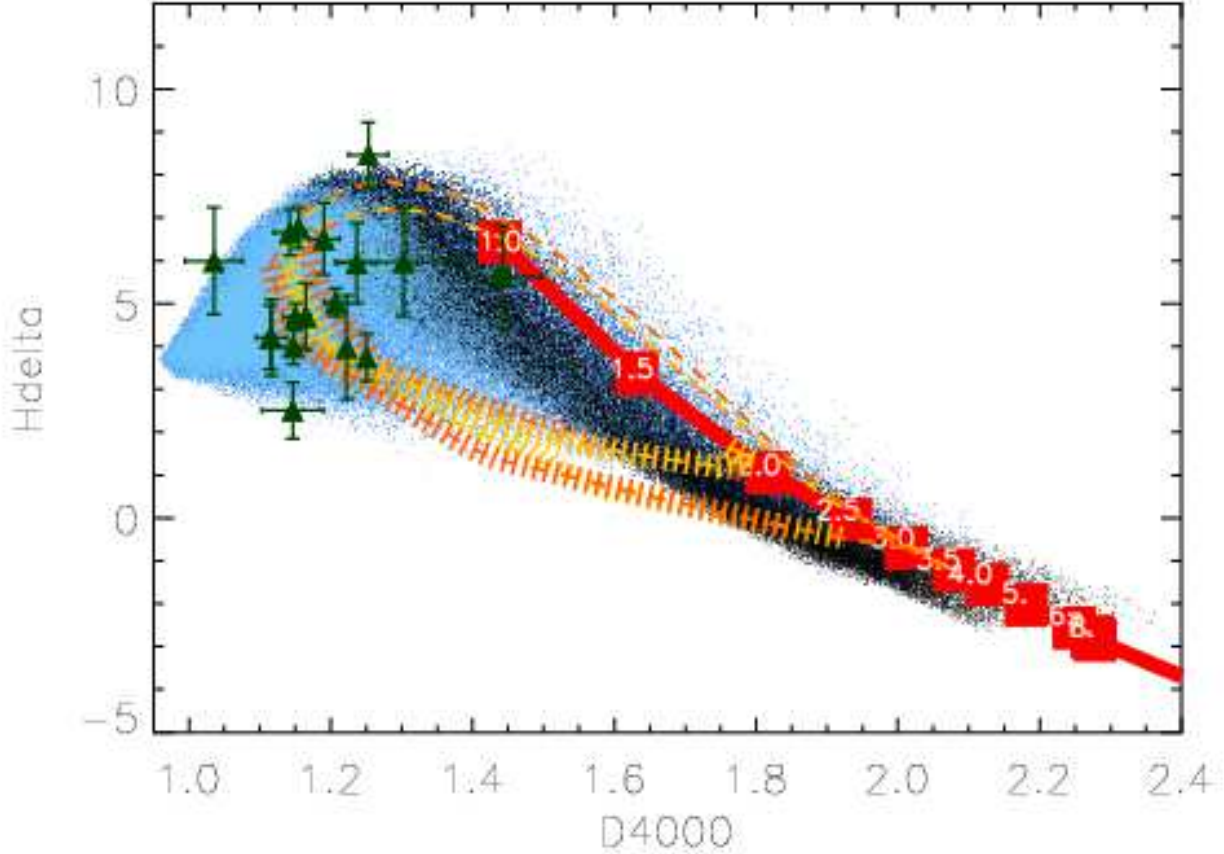


Fig. 9. Location of the 200,000 Monte Carlo realizations using the parameters of SIM2 (see table 5) in the $H\delta_A$ versus 4000 \AA (D4000) break diagram. **Light blue points (lower-left):** starbursting galaxies. **Dark blue points (upper part):** post-starburst galaxies (galaxies having experienced a recent starburst which ended less than 2 Gyr ago). **Black points:** galaxies with a continuous star formation in the two past Gyears. **Bold red line:** track followed by an individual galaxy with continuous star formation (numbers in squares = age in Gyr) generated with GALAXEV ($\gamma=4.$, $\mu=0.3$, $\tau_V=3.0$, $V_{\text{disp}}=200 \text{ km.s}^{-1}$). **Orange loops:** effect of starbursts of 5×10^7 (dashed line) and 10^8 (plain line) years starting after 2 Gyr (light orange) and 3 Gyr (dark orange) of continuous star formation. The line is hatched during the starburst phase. The size of the orange dots is proportional to the time counted in 10^8 years units after the beginning of the burst. **Triangles:** galaxies corrected for the underlying nebular emission line in $H\delta_A$ as derived from the observed lower order Balmer lines corrected for attenuation from the Balmer lines ratio. **Stars:** galaxies with negligible emission Balmer line in emission, hence uncorrected for $H\delta_A$ emission. **Squares:** corrected for the underlying $H\delta_A$ emission line using only one Balmer emission line available with dust attenuation computed from the IR (from the ratio of $\text{SFR}(\text{IR})$ over $\text{SFR}(H\beta)$). **Circles:** no correction for the underlying potential emission line because no information is available on the Balmer emission lines.

6.3. Determination of the burst duration

In the $H\delta_A$ -D4000 diagram, the burst duration, τ_B , can be constrained for 11 galaxies (Table 6) for which we obtain a median of $\tau_B = 1.3_{-0.5}^{+1.9} \times 10^8$ years, e.g. Fig. 10b. Using H8, the technique converges for 14 galaxies to $\tau_B = 1.0_{-0.6}^{+1.6} \times 10^8$ years. Here again, as for the Scalo parameter in the previous section, we find a consistent result using both H8 and $H\delta_A$. Both indicate that the bursts are short-lived over about 0.1 Gyr. The large dispersion between the various galaxies may result from different initial gas mass fractions or triggering mechanisms for the burst.

6.4. Determination of the burst stellar mass fraction

The simulations converge to a value of f_B for only 6/22 galaxies in the H8-D4000 diagram and 10/17 in the $H\delta_A$ -D4000 (see the example of UDSR 23 in Fig. 10c). The difficulty to determine the burst stellar mass fraction is not surprising. It results from the fact that as soon as the young stellar population starts dominating the spectrum of a galaxy, it becomes nearly impossible to measure with good precision the fraction of the light due to the underlying older population. Indeed, the PDFs converge only for galaxies for which the fraction of young stars remains low (see Tables 6,7).

id	SFR/<SFR> (%) [68 %]	τ_B [τ_B^-, τ_B^+] $\times 0.1$ Gyr [68 %]	f_B [f_B^-, f_B^+] (%) [68 %]	f_B^{eff} [$f_B^{\text{eff}-}, f_B^{\text{eff}+}$] (%) [68 %]
UDSF06	–	2 [1,6]	3 [2,19]	3 [2,22]
UDSF07	4 [2,13]	0.2 [0.1,0.9]	–	–
UDSF12	–	≥ 8.9	–	–
UDSF17	–	5 [1,8]	–	–
UDSF19	–	–	2 [1,15]	3 [2,19]
UDSF28	4 [2,8]	–	–	–
UDSF29b	–	–	–	–
UDSF20	2 [1,5]	–	–	–
UDSF31	–	–	–	–
UDSR08	7 [3,30]	0.4 [0.2,0.7]	–	–
UDSR09	–	0.4 [0.2,0.9]	–	–
UDSR10	–	1 [0.3,2.2]	3 [2,13]	3 [3,15]
UDSR14	5 [2,12]	0.8 [0.3,1.7]	–	–
UDSR20	–	7 [3,8]	–	–
UDSR23	3 [2,7]	1 [1,3]	–	–
CFRS02	–	≥ 3.1	–	–
CFRS06	3 [1,7]	0.2 [0.1,0.7]	4 [3,13]	4 [3,16]
CFRS08	4 [2,10]	0.4 [0.1,1.0]	3 [2,11]	4 [3,14]
CFRS10	8 [5,14]	1.0 [0.6,2.0]	–	–
CFRS14	4 [2,11]	0.6 [0.3,1.6]	–	–
CFRS16	7 [3,23]	≤ 7.85	4 [2,18]	5 [3,21]
CFRS29	3 [2,9]	2.5 [1,5]	–	–

Table 7. Results concerning the burst duration, the Scalo ratio SFR/<SFR>, and the burst fraction (f_B) when using the H8 data.

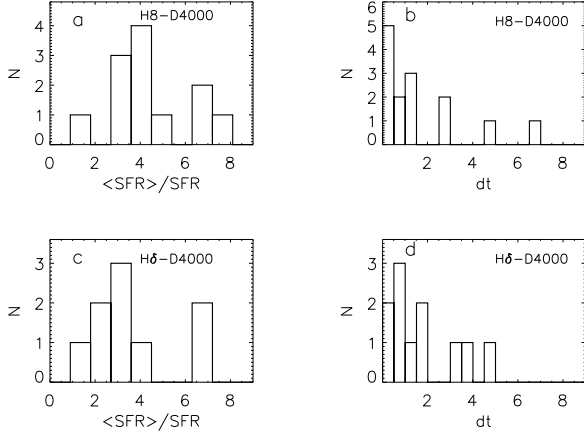


Fig. 11. Distribution of the Scalo parameter and the burst duration. a) The Scalo parameter in the H8-D4000 diagram. b) The burst duration in the H8-D4000 diagram. c) The Scalo parameter in the $H\delta_A$ -D4000 diagram. d) The burst duration in the $H\delta_A$ -D4000 diagram.

However, we can still derive the effective burst stellar mass fraction, f_B^{eff} , which is equal to the mass of stars produced during the burst, i.e. $\tau_B \times \text{SFR}$, divided by the total stellar mass of the galaxy, i.e. $t_{\text{form}} \times \langle \text{SFR} \rangle$. Since $\tau_B = 1.0^{+1.6}_{-0.6} \times 10^8$ years and $\text{SFR} = 52^{+34}_{-33} M_{\odot} \text{ yr}^{-1}$, we obtain an effective burst stellar mass fraction of $f_B^{\text{eff}} = 10 \pm 9\%$. Note that a burst producing 10% of a $7 \times 10^{10} M_{\odot}$ galaxy, will convert $7 \times 10^9 M_{\odot}$ of molecular gas into stars, which is consistent with the mass of

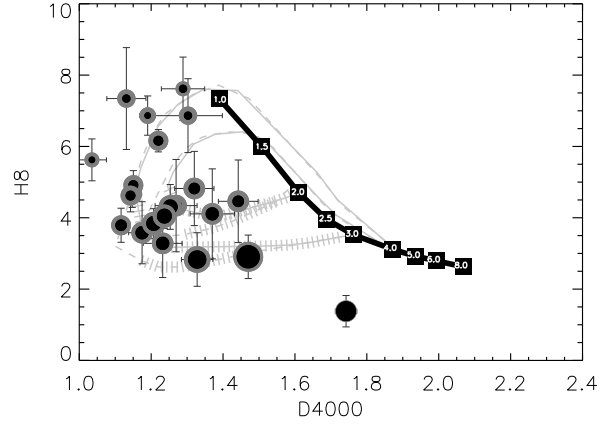


Fig. 12. The lines are the same as in Fig. 7 and in Fig. 8. The black circle are proportional to t_{20} defined before, while the grey one to t_{50} .

molecular gas observed in local LIRGs and ULIRGs (Sanders & Mirabel 1996).

6.5. Testing the "multiple burst" scenario

A sub-sample of the distant LIRGs lie on the upper-left part of the H8 and $H\delta_A$ versus D4000 diagrams (Figs. 8, 9). This region is populated by Monte Carlo realizations of galaxies for which the ongoing burst of star formation was superimposed on a previous burst which ended less than 2 Gyr ago. In order to quantify the probability of such an occurrence, we gener-

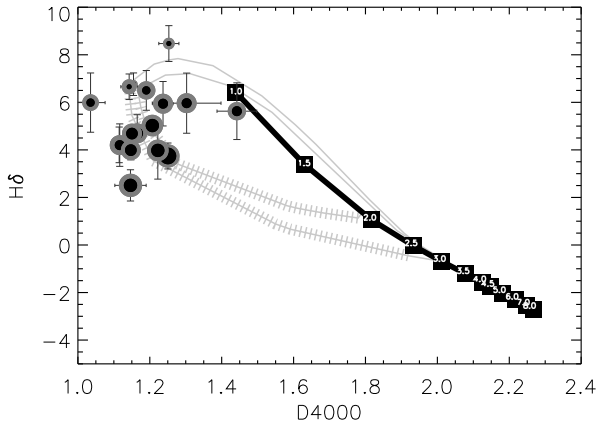


Fig. 13. The lines are the same as in Fig. 7 and in Fig. 8. The black circle are proportional to t_{20} defined before, while the grey one to t_{50} .

id	t_{20} 10 ⁸ years	t_{50} 10 ⁸ years
(1)	(2)	(3)
6.udsf	7.0	13.0
7.udsf	8.0	13.0
12.udsf	5.0	9.0
17.udsf	6.0	12.0
19.udsf	7.0	13.0
28.udsf	14.0	18.0
29.udsf	8.0	13.0
20.udsf	11.0	16.0
31.udsf	7.0	13.0
8.udsr	7.0	12.0
10.udsr	9.0	14.0
14.udsr	7.0	12.0
20.udsr	4.0	10.0
23.udsr	6.0	12.0
9.udsr	12.0	13.0
2.cfrs	5.0	11.0
6.cfrs	9.0	14.0
8.cfrs	9.0	14.0
10.cfrs	4.0	9.0
14.cfrs	6.0	12.0
16.cfrs	8.0	13.0
29.cfrs	5.0	11.0

Table 8. Values of t_{20} (black circle) and t_{50} (grey circle) obtained for the 22 galaxies in the H8-D4000 diagram, to quantify the probability of two successive starbursts (see text).

ated a third simulation, SIM3, in which half of the realizations experienced two successive bursts during the last 2 Gyr. We then computed for each galaxy, using the same bayesian statistics, a probability for various possible durations between the two bursts. Two representative numbers are assigned for each galaxy in Tables 8 and 9: t_{20} and t_{50} . These values correspond to lookback times associated with a 20 and 50 % chance of finding a previous burst which ended t_{20} and t_{50} Gyr before the onset

id	t_{20} 10 ⁸ years	t_{50} 10 ⁸ years
(1)	(2)	(3)
7.udsf	6.0	11.0
16.udsf	10.0	14.0
17.udsf	3.0	5.0
18.udsf	7.0	12.0
19.udsf	8.0	13.0
31.udsf	6.0	11.0
8.udsr	6.0	12.0
10.udsr	3.0	7.0
14.udsr	7.0	12.0
20.udsr	5.0	11.0
23.udsr	7.0	12.0
2.cfrs	6.0	12.0
6.cfrs	8.0	13.0
8.cfrs	6.0	12.0
10.cfrs	5.0	10.0
11.cfrs	8.0	14.0
14.cfrs	3.0	9.0

Table 9. Values of t_{20} (black circle) and t_{50} (grey circle) obtained for the 17 galaxies in the H δ_A -D4000 diagram, to quantify the probability of two successive starbursts (see text).

of the ongoing one. For example, in the case of UDSR20, we obtain from the H8-D4000 diagram (see Table 8) $t_{20} = 0.4$ Gyr and $t_{50} = 1$ Gyr, which implies that there is a 50 % chance that a previous starburst occurred 1 Gyr before the onset of the present one and a 20 % chance that the delay was only a 0.4 Gyr. Hence UDSR20 is a good candidate for two successive bursts. We did not consider higher probabilities or longer timescales because of the limited constraints that we can set on those parameters and because after about 1.5 Gyr, the memory of the previous burst is lost with this technique.

Local LIRGs and ULIRGs are known to be predominantly triggered by major mergers (Borne et al. 1999, Sanders & Mirabel 1996) and numerical simulations of such mergers predict that the two galaxies cross each other several times, potentially inducing a series of bursts separated by a few tens of million years (Mihos & Hernquist 1996). However, in distant LIRGs, the probability that a previous starburst occurred less than 0.5 Gyr ago is nearly always lower than 20 %. This result must be considered together with recent evaluations of the morphological properties of distant LIRGs which also suggest that most of them are not produced in major mergers (Bell et al. 2005, Zheng et al. 2004, Elbaz & Cesarsky 2004). Bell et al. (2005) suggested that distant LIRGs could either be non-triggered phases in isolated spirals with larger gas masses, possibly experiencing some infall, or minor mergers, where the dwarf galaxy responsible is not detected. Our determination of a burst duration of 0.1 Gyr and a Scalo parameter of 4, seems to rule out the possibility that distant LIRGs are isolated spirals forming stars at a constant rate over a long duration. The starbursts may instead be triggered by tidal effects and minor mergers in regions of the universe where the local density of galaxies is enhanced as suggested by Elbaz & Cesarsky (2003)

or by the infall of intergalactic gas (Combes, 2005). Further kinematical studies of distant galaxies (see Flores et al, 2006; Puech et al, 2006) will help to distinguish between the various scenarios (mergers, gas infall) discussed here.”

7. Discussion and conclusions

We have analyzed the star formation history of a sample of 25 distant LIRGs ($\bar{z} = 0.7$) that we derived from their stellar spectra (Balmer absorption lines and 4000 Å break). The high order Balmer absorption line H8 and the $H\delta_A$ line provide consistent results although H8 is more adapted to distant galaxies being located in a bluer region of the spectrum, less affected by sky emission lines and which is measured for more distant objects than $H\delta_A$. Variations at the 30% level between the burst parameters obtained using one or the other indicator suggest that some effects, such as abundance ratios which might affect the pseudo-continua surrounding the $H\delta_A$ line, should be taken into account to improve the models (see Thomas, Maraston & Korn 2004, Korn, Maraston & Thomas 2005).

The comparison of distant LIRGs, selected from ISOCAM and MIPS, onboard ISO and Spitzer, to local LIRGs, selected from IRAS and the SDSS, shows that both populations present similar spectral features and therefore suggests that they are experiencing comparable starburst phases. The fact that half of the local LIRGs present D4000 values larger than the maximum D4000 of distant LIRGs indicates that the dominant non bursting stellar population is younger for distant LIRGs, as expected.

The first important result of this study is the identification of an optical signature for the presence of a starburst in these galaxies, in spite of their large dust attenuation. While continuous star formation follows a line along decreasing Balmer EW and increasing D4000, a burst superimposed on this population produces a loop that first decrease D4000 and then increase the Balmer line EW. However, after about 1.5 Gyr, the memory of the burst is lost and the galaxy behaves like others which did not experience a starburst. As result, we are limited to study only the averaged past star formation history for look-back times shorter than 1.5 Gyr. The bursts characteristics were derived from probability distribution functions (PDF) using a bayesian statistics as in Kauffmann et al. (2003).

The median ratio of present over averaged SFR, the so-called Scalo parameter, for the distant LIRGs is $\text{SFR}/\langle\text{SFR}\rangle = 4 \pm 1$ (we used the H8 line for which a larger sample of galaxies is available and the PDFs present a sharper peak), which indicates that these galaxies are experiencing an atypically intense phase of star formation in their lifetime. A median SFR of $52^{+34}_{-33} M_{\odot} \text{ yr}^{-1}$ for the ongoing starbursts was derived from their MIR luminosities. Hence, their mean SFR averaged over their lifetime is $\langle\text{SFR}\rangle = 13 \pm 3 M_{\odot} \text{ yr}^{-1}$. Knowing the median stellar mass for LIRGs of equivalent luminosity and redshift range (from Franceschini et al. 2003), we derived an age for those distant LIRGs of $t_{\text{form}} = 5.5 \pm 1.5$ Gyr, suggesting that they formed at $z_{\text{form}} = 4.5 \pm 1.5$.

As for the bursts themselves, we computed a median duration of $\tau_B = 1.0^{+1.6}_{-0.6} \times 10^8$ years, during which the galaxies produced $10 \pm 9\%$ (the error bar includes 68% of the galaxy

sample) of their stellar mass. This corresponds to a mass of molecular gas of about $7 \times 10^9 M_{\odot}$ which is consistent that observed in local LIRGs and ULIRGs (see Sanders & Mirabel 1996).

We note that all simulations produced in this paper assume the same fixed IMF for both the underlying star formation and the burst of star formation. Some evidence that the formation of low-mass may be less efficient in the environment of active star formation in the solar neighborhood were suggested in the past (Larson 1986, Scalo 1986, Maeder 1993). A top-heavy IMF could also account for the enhanced ratio of light elements to iron in massive early-type galaxies (Worthey, Faber & Gonzalez 1992) and for the relative enrichment of oxygen to iron in the intra-cluster medium (Arnaud et al, 1992). In our study, the occurrence of a top-heavy IMF in the burst episode would only weakly influence the derived burst duration timescales, which are set by the spectral signature of massive A to F stars. However, a top-heavy IMF during the burst phase would imply a much lower contribution to the total galaxy mass by longer-lived, low-mass stars.

Finally, we discussed the possibility that the distant LIRGs experienced a previous starburst prior to the ongoing one during the last 1.5 Gyr. While most galaxies are not consistent with a merger scenario where two galaxies merge in several phases producing a series of bursts separated by a few ten millions years (Mihos & Hernquist 1996), the majority present more than 50% chance to have experienced a previous burst in the last 1.5 Gyr, i.e. since $z \sim 1$. If these properties are typical of LIRGs between $z = 1$ and $z = 0$, then this suggests that the population of galaxies experiencing LIRG phases experienced on average 2 to 3 LIRG phases since $z = 1$ and up to 4 since their birth around $z = 4-5$, as also suggested by Hammer et al. (2005). This scenario is not consistent with the formation of distant LIRGs through the continuous star formation characterizing isolated spiral galaxies as has been argued independently based on their morphology. Instead, minor mergers, tidal interactions and gas accretion all remain equally plausible triggering mechanisms for more than half of the distant LIRGs which do not harbor the morphology of major mergers.

Acknowledgements. We wish to thank the anonymous referee for his constructive remarks which helped improving the paper in particular on the wavelet analysis. We also wish to thank Anna Gallazzi, Nicolas Gruel, Emmanuel Moy and Jean Luc Starck for helpful discussions and comments and Emeric Le Floch for technical support for MIPS data. S.C. thanks the Alexander von Humboldt Foundation, the Federal Ministry of Education and Research, and the Programme for Investment in the Future (ZIP) of the German Government for their support.

References

- Arnaud, M., Rothenflug, R., Boulade, O., Vigroux, L., & Vangioni-Flam, E. 1992, A&A, 254, 49
- Balogh, M. L., Morris, S. L., Yee, H. K. C., Carlberg, R. G., & Ellingson, E. 1999, ApJ, 527, 54
- Bell, E. F., Papovich, C., Wolf, C., et al. 2005, ApJ, 625, 23
- Bica, E. & Alloin, D. 1986, A&A, 162, 21
- Blain, A. W., Kneib, J.-P., Ivison, R. J., & Smail, I. 1999, ApJ, 512, L87

- Borne, K. D., Colina, L., Bushouse, H., & Lucas, R. A. 1999, *ApJ*, 527, 554
- Borne, K. D. & et al. 1999, in *ASP Conf. Ser. 177: Astrophysics with Infrared Surveys: A Prelude to SIRTF*, 167–+
- Bruzual, G. & Charlot, S. 2003, *MNRAS*, 344, 1000
- Bruzual A., G. 1983, *ApJ*, 273, 105
- Cardiel, N., Elbaz, D., Schiavon, R. P., et al. 2003, *ApJ*, 584, 76
- Charlot, S. & Fall, S. M. 2000, *ApJ*, 539, 718
- Chary, R., Casertano, S., Dickinson, M. E., et al. 2004, *ApJS*, 154, 80
- Chary, R. & Elbaz, D. 2001, *ApJ*, 556, 562
- Combes, F. 2005, in *AIP Conf. Proc. 783: The Evolution of Starbursts*, ed. S. Hüttmeister, E. Manthey, D. Bomans, & K. Weis, 43–49
- Dale, D. A. & Helou, G. 2002, *ApJ*, 576, 159
- Elbaz, D., Cesarsky, C. J., Chanical, P., et al. 2002, *A&A*, 384, 848
- Elbaz, D., Le Floc'h, E., Dole, H., & Marcillac, D. 2005, *A&A*, 434, L1
- Fadda, D., Flores, H., Hasinger, G., et al. 2002, *A&A*, 383, 838
- Flores, H., Hammer, F., Elbaz, D., et al. 2004, *A&A*, 415, 885
- Flores, H., Hammer, F., Puech, M., Amram, P., & Balkowski, C. 2006, accepted in *A&A*
- Franceschini, A., Berta, S., Rigopoulou, D., et al. 2003, *A&A*, 403, 501
- Gorgas, J., Cardiel, N., Pedraz, S., & González, J. J. 1999, *A&AS*, 139, 29
- Hammer, F., Flores, H., Elbaz, D., et al. 2005, *A&A*, 430, 115
- Hopkins, A. M., Miller, C. J., Nichol, R. C., et al. 2003, *ApJ*, 599, 971
- Kauffmann, G., Heckman, T. M., White, S. D. M., et al. 2003, *MNRAS*, 341, 33
- Kim, D.-C. & Sanders, D. B. 1998, *ApJS*, 119, 41
- Korn, A. J., Maraston, C., & Thomas, D. 2005, *A&A*, 438, 685
- Lagache, G. & Dole, H. 2001, *A&A*, 372, 702
- Lagache, G., Puget, J. L., & Dole, H. 2005, accepted in *MNRAS*
- Larson, R. B. 1986, in *Stellar Populations*, 101–119
- Le Borgne, J.-F., Bruzual, G., Pelló, R., et al. 2003, *A&A*, 402, 433
- Le Floc'h, E., Papovich, C., Dole, Bell, E., et al. 2005, accepted in *ApJS*
- Liang, Y. C., Hammer, F., Flores, H., et al. 2005, *Chinese Journal of Astronomy and Astrophysics*, 5, 335
- Liang, Y. C., Hammer, F., Flores, H., et al. 2004, *A&A*, 423, 867
- Maeder, A. 1993, in *The Feedback of Chemical Evolution on the Stellar Content of Galaxies*, 173
- Marano, B., Zamorani, G., & Zitelli, V. 1988, *MNRAS*, 232, 111
- Marcillac, D., Elbaz, D., Chary, R. R., et al. 2005, accepted in *A&A*
- Mihos, J. C. & Hernquist, L. 1996, *ApJ*, 464, 641
- Osterbrock, D. E. 1989, *S&T*, 78, 491
- Papovich, C., Dole, H., Egami, E., et al. 2004, *ApJS*, 154, 70
- Pasquali, A., Kauffmann, G., & Heckman, T. M. 2005, *MNRAS*, 361, 1121
- Poggianti, B. M. & Barbaro, G. 1997, *A&A*, 325, 1025
- Puech, M., Flores, H., Hammer, F., & Lehnert, M. D. 2006, *ArXiv Astrophysics e-prints*
- Puget, J. L., Lagache, G., Clements, D. L., et al. 1999, *A&A*, 345, 29
- Scalo, J. M. 1986, *Fundamentals of Cosmic Physics*, 11, 1
- Smail, I., Kuntschner, H., Kodama, T., et al. 2001, *MNRAS*, 323, 839
- Soifer, B. T. & Neugebauer, G. 1991, *AJ*, 101, 354
- Starck, J.-L. & Murtagh, F. 1994, *A&A*, 288, 342
- Starck, J. L., Pantin, E., & Murtagh, F. 2002, *PASP*, 114, 1051
- Stetson, P. B. & Aikman, C. L. 1987, *AJ*, 93, 1439
- Thomas, D., Maraston, C., & Korn, A. 2004, *MNRAS*, 351, L19
- Worthey, G., Faber, S. M., & Gonzalez, J. J. 1992, *ApJ*, 398, 69
- Worthey, G. & Ottaviani, D. L. 1997, *ApJS*, 111, 377
- Zamorani, G., Mignoli, M., Hasinger, G., et al. 1999, *A&A*, 346, 731
- Zheng, X. Z., Hammer, F., Flores, H., Assémat, F., & Pelat, D. 2004,